

Measurement of the $e^+e^- \rightarrow \pi^+\pi^-\pi^0$ cross section in the energy region from 0.56 to 1.1 GeV with the SND detector

M. N. Achasov,^{1,2} A. E. Alizzi,^{1,2} A. Yu. Barnyakov,¹ K. I. Beloborodov,^{1,2}
A. V. Berdyugin,^{1,2} D. E. Berkaev,^{1,2} A. G. Bogdanchikov,¹ A. A. Botov,¹ V. S. Denisov,¹
T. V. Dimova,^{1,2} V. P. Druzhinin,^{1,2,*} R. A. Efremov,^{1,3} E. A. Eminov,¹ L. B. Fomin,¹
L. V. Kardapoltsev,^{1,2} A. A. Kattsin,¹ A. G. Kharlamov,^{1,2} I. A. Koop,^{1,2} A. A. Korol,^{1,2}
D. P. Kovrizhin,¹ A. S. Kupich,^{1,2} A. P. Kryukov,¹ N. A. Melnikova,¹ N. Yu. Muchnoi,^{1,2}
A. E. Obrazovsky,¹ A. A. Oorzhak,^{1,2} I. V. Ovtin,^{1,2} E. V. Pakhtusova,¹
E. A. Perevedentsev,^{1,2} I. A. Polomoshnov,^{1,2} K. V. Pugachev,^{1,2} Yu. A. Rogovsky,^{1,2}
V. A. Romanov,^{1,2} S. I. Serednyakov,^{1,2} Yu. M. Shatunov,¹ D. A. Shtol,¹ Z. K. Silagadze,^{1,2}
K. D. Sungurov,^{1,2} M. V. Timoshenko,¹ I. K. Surin,¹ Yu. V. Usov,¹ I. M. Zemlyansky,¹
V. N. Zhabin,^{1,2} Yu. M. Zharinov,¹ V. V. Zhulanov,^{1,2} and P. V. Zhulanova^{1,2}

¹*Budker Institute of Nuclear Physics,*

SB RAS, Novosibirsk, 630090, Russia

²*Novosibirsk State University, Novosibirsk, 630090, Russia*

³*Novosibirsk State Technical University, Novosibirsk, 630073, Russia*

The precise measurement of the $e^+e^- \rightarrow \pi^+\pi^-\pi^0$ cross section is performed in the center-of-mass energy range $E = 560\text{--}1100$ MeV using a data sample of 66 pb⁻¹ collected in the experiment with the SND detector at the VEPP-2000 e^+e^- collider. The systematic uncertainty of the cross section measurement is 0.9% at the maximum of the ω resonance and 1.2% at the maximum of the ϕ resonance. The leading-order hadronic contribution to the muon magnetic anomaly calculated using the $e^+e^- \rightarrow \pi^+\pi^-\pi^0$ cross section measured by SND from 0.62 to 1.975 GeV is $(45.95 \pm 0.06 \pm 0.46) \times 10^{-10}$. From the fit to the cross section data with the vector meson dominance model, the parameters of the ω , ρ , and ϕ resonances are obtained. The obtained values of $\mathcal{B}(\omega \rightarrow e^+e^-)\mathcal{B}(\omega \rightarrow 3\pi)$, mass and width of the ω meson, and $\mathcal{B}(\rho \rightarrow 3\pi)$ have accuracy better than the current world average values.

*Electronic address: druzhinin@inp.nsk.su

I. INTRODUCTION

This article is devoted to the measurement of the $e^+e^- \rightarrow \pi^+\pi^-\pi^0$ cross section in the center-of-mass energy range of $0.56 < E < 1.1$ GeV in the experiment with the SND detector at the VEPP-2000 collider [1]. In this energy range, the cross section is dominated by the contributions of the ω and ϕ resonances.¹ From the approximation of the cross section in the vector meson dominance (VMD) model, the parameters of these resonances, as well as the branching fraction of the isospin-violating decay $\rho \rightarrow \pi^+\pi^-\pi^0$, can be extracted. Below 1 GeV, the $e^+e^- \rightarrow \pi^+\pi^-\pi^0$ cross section is the second largest cross section after $e^+e^- \rightarrow \pi^+\pi^-$. Therefore, its measurement is important for the Standard Model calculation of the muon anomalous magnetic moment (see, for example, Ref. [2]).

The most accurate measurements of the cross section for the $e^+e^- \rightarrow \pi^+\pi^-\pi^0$ process in the energy range under study were performed in the CMD-2 [3, 4] and SND [5, 6] experiments at the VEPP-2M e^+e^- collider, as well as by the radiative return method in the BABAR [7] and Belle II [8] experiments. There are significant discrepancies between the data from these experiments. For example, in the region near the maximum of the ω resonance the cross section measured by Belle II is approximately 8% larger than the BABAR cross section, with declared systematic uncertainties of 2.3% and 1.3%, respectively. Obviously, a new measurement of the $e^+e^- \rightarrow \pi^+\pi^-\pi^0$ cross section with an accuracy of no worse than 1.5% is required to clarify the experimental situation.

II. SND DETECTOR

The Spherical Neutral Detector (SND) [9–12] (Fig. 1) is a general-purpose non-magnetic detector operating at the VEPP-2000 e^+e^- collider [1] with the c.m. energy $E = 0.32 - 2$ GeV. It consists of a tracking system, a system of aerogel threshold Cherenkov counters, an electromagnetic calorimeter, and a muon system. The tracking system is a nine-layer drift chamber and a single-layer proportional chamber with cathode strip readout located in a common gas volume. Its angular resolution is 0.45° for azimuthal angle and 0.8° for polar angle. The reconstructed charged track must contain at least 4 hits in the drift chamber. The tracking system solid angle for charged particles originating from the collider interaction

¹ Throughout this paper, the notation ρ , ω , and ϕ is used for $\rho(770)$, $\omega(782)$, and $\phi(1020)$.

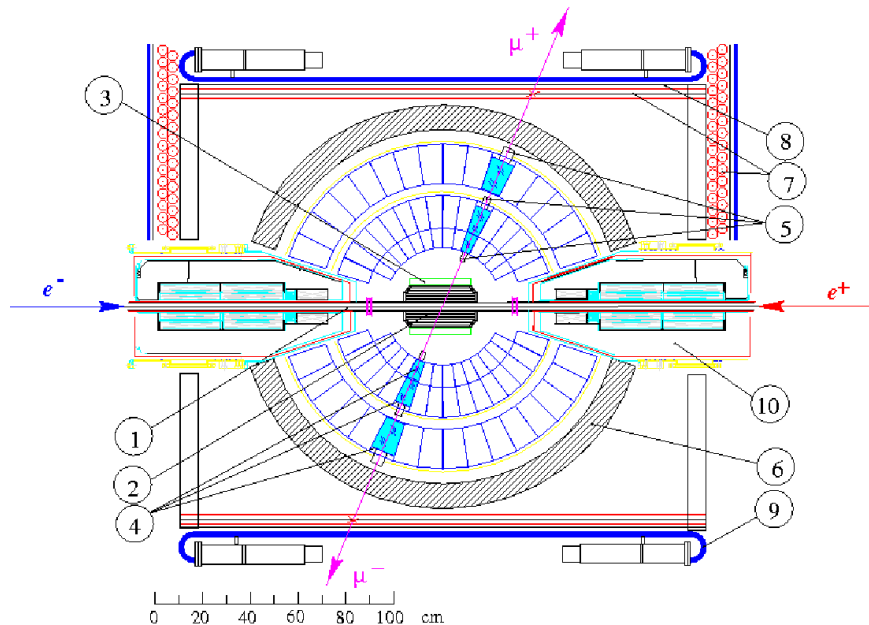


FIG. 1: SND detector, section along the beams: (1) beam pipe, (2) tracking system, (3) aerogel Cherenkov counters, (4) NaI (Tl) crystals, (5) vacuum phototriodes, (6) iron absorber, (7) proportional tubes, (8) iron absorber, (9) scintillation counters, (10) VEPP-2000 focusing solenoids.

region is 94% of 4π . The Cherenkov counters are located around the tracking system. They use aerogel with the refractive index of 1.05 allowing for the pion identification at momenta below $436 \text{ MeV}/c$. This system covers 60% of the total solid angle. The three-layer spherical electromagnetic calorimeter, based on NaI (Tl) crystals, covers 95% of the solid angle. It is used, in particular, to identify photons, which are defined as clusters of adjacent crystals in the calorimeter with energy depositions exceeding 20 MeV and no associated charged tracks. The calorimeter energy resolution for photons is $4.2\%/\sqrt[4]{E(\text{GeV})}$, and the angular resolution is about 1.5° . The muon system is located outside the calorimeter and consists of proportional tubes and scintillation counters.

The Monte-Carlo (MC) event generator for the signal process $e^+e^- \rightarrow \pi^+\pi^-\pi^0$ uses a model with an intermediate $\rho\pi$ state, which works well at the ω and ϕ resonances [13, 14]. Generators for signal and background hadronic ($e^+e^- \rightarrow \pi^+\pi^-\pi^0$, K^+K^- , $K_S K_L$, $\omega\pi^0$, $\eta\gamma$, $\pi^0\gamma$) events takes into account radiative corrections [15]. The angular distribution of a hard photon emitted from the initial state is generated according to Ref. [16]. The final-state radiation for the signal process is simulated using the PHOTOS package [17]. The background $e^+e^- \rightarrow \pi^+\pi^-(\gamma)$ events are simulated with the MCGPJ event generator [18].

To simulate backgrounds from the QED processes $e^+e^- \rightarrow e^+e^-\gamma(\gamma)$ and $e^+e^- \rightarrow \mu^+\mu^-\gamma(\gamma)$, the event generator BabaYaga@NLO [19] is used. Interactions of the particles produced in e^+e^- annihilation with the detector materials are simulated using the GEANT4 software [20]. The simulation takes into account variation of experimental conditions during data taking, in particular dead detector channels and beam-induced background. To take into account the effect of superimposing the beam background on the e^+e^- annihilation events, the simulation uses special background events recorded during data taking with a random trigger. These events are superimposed on the simulated events, leading to the appearance of additional tracks and photons in them.

In this article, a data sample, collected with the SND detector at the VEPP-2000 e^+e^- collider in 2018 in the energy range $E = 560\text{--}1100$ MeV, is analyzed. The integrated luminosity accumulated at 102 energy points is about 66 pb^{-1} .

During data taking, the average beam energy and the energy spread were measured by a dedicated system using the Compton back-scattering of laser photons on the electron beam [21]. The systematic uncertainty of the energy measurement by this method was estimated in Ref. [21] by comparison with the measurement by the resonance depolarization method at $E_b = 510$ and 460 MeV, where E_b is the beam energy. It is found to be $\Delta E_b/E_b = 6 \times 10^{-5}$. Energy measurements performed at a given energy point are averaged with weights proportional to the integrated luminosity. The obtained values for average energy, energy spread σ_E and their errors are listed in Table I. The error of the measured energy (δE) includes the statistical error and the uncertainty due to the beam energy drift during data taking. The systematic error of σ_E does not exceed 5%.

The integrated luminosity is measured using $e^+e^- \rightarrow e^+e^-$ events. The procedure for selecting e^+e^- events, subtracting $\pi^+\pi^-$, $\mu^+\mu^-$ backgrounds, and analyzing various sources of systematic uncertainties in determining the number of e^+e^- events is described in detail in Ref. [22]. The distribution of the integrated luminosity over energy points is given in Table I. Only the statistical error is quoted. The systematic uncertainty does not exceed 0.7%.

TABLE I: The center-of-mass energy (E), its spread (σ_E), and integrated luminosity (IL).

E , MeV	σ_E , keV	IL , pb $^{-1}$	E , MeV	σ_E , keV	IL , pb $^{-1}$
560.237 \pm 0.007	152 \pm 8	52.7 \pm 0.2	787.811 \pm 0.007	282 \pm 6	1204.9 \pm 2.4
570.215 \pm 0.005	134 \pm 6	76.1 \pm 0.3	788.023 \pm 0.011	267 \pm 10	213.9 \pm 0.7
580.145 \pm 0.005	136 \pm 6	87.2 \pm 0.3	790.133 \pm 0.016	245 \pm 15	220.4 \pm 0.7
590.206 \pm 0.009	129 \pm 14	61.6 \pm 0.3	791.856 \pm 0.009	315 \pm 6	655.3 \pm 1.5
600.151 \pm 0.005	152 \pm 6	91.6 \pm 0.3	792.108 \pm 0.014	251 \pm 13	194.9 \pm 0.7
610.068 \pm 0.006	139 \pm 7	64.6 \pm 0.3	794.047 \pm 0.019	289 \pm 18	221.2 \pm 0.7
620.167 \pm 0.008	175 \pm 7	82.4 \pm 0.3	796.067 \pm 0.019	266 \pm 17	237.0 \pm 0.7
630.085 \pm 0.010	160 \pm 13	82.6 \pm 0.3	797.955 \pm 0.016	225 \pm 17	163.8 \pm 0.6
640.019 \pm 0.007	170 \pm 5	83.1 \pm 0.3	800.668 \pm 0.011	231 \pm 11	226.3 \pm 0.7
650.612 \pm 0.011	207 \pm 13	82.6 \pm 0.3	810.583 \pm 0.008	222 \pm 8	338.3 \pm 0.9
660.328 \pm 0.022	188 \pm 21	83.0 \pm 0.3	820.284 \pm 0.009	238 \pm 7	353.1 \pm 1.0
670.201 \pm 0.015	203 \pm 15	83.7 \pm 0.3	829.859 \pm 0.015	268 \pm 13	226.2 \pm 0.7
679.781 \pm 0.270	237 \pm 30	2942.8 \pm 4.8	840.025 \pm 0.013	257 \pm 10	196.1 \pm 0.7
689.880 \pm 0.260	240 \pm 20	286.6 \pm 0.7	850.553 \pm 0.013	239 \pm 13	268.3 \pm 0.8
699.860 \pm 0.170	250 \pm 30	242.3 \pm 0.6	860.252 \pm 0.012	238 \pm 10	174.4 \pm 0.7
709.969 \pm 0.008	238 \pm 8	190.8 \pm 0.6	870.291 \pm 0.010	272 \pm 9	267.9 \pm 0.9
719.930 \pm 0.050	274 \pm 10	2363.6 \pm 3.6	880.194 \pm 0.015	273 \pm 14	217.2 \pm 0.8
723.798 \pm 0.023	307 \pm 19	144.8 \pm 0.5	889.788 \pm 0.022	255 \pm 20	239.4 \pm 0.8
727.733 \pm 0.020	286 \pm 14	124.1 \pm 0.5	899.816 \pm 0.034	271 \pm 12	298.0 \pm 0.9
731.994 \pm 0.017	310 \pm 13	116.9 \pm 0.5	909.399 \pm 0.018	383 \pm 13	1376.8 \pm 2.8
736.202 \pm 0.031	310 \pm 9	167.9 \pm 0.6	910.112 \pm 0.011	260 \pm 10	173.3 \pm 0.7
739.948 \pm 0.013	225 \pm 13	139.0 \pm 0.5	920.282 \pm 0.012	362 \pm 7	916.9 \pm 2.1
744.089 \pm 0.012	202 \pm 13	129.1 \pm 0.5	920.685 \pm 0.039	260 \pm 11	223.9 \pm 0.8
748.048 \pm 0.012	218 \pm 11	148.5 \pm 0.5	921.726 \pm 0.019	326 \pm 15	282.9 \pm 0.9
750.019 \pm 0.050	295 \pm 10	5484.9 \pm 6.2	929.637 \pm 0.012	356 \pm 8	1461.5 \pm 3.0
751.989 \pm 0.014	251 \pm 10	118.9 \pm 0.5	930.427 \pm 0.020	295 \pm 17	271.1 \pm 0.9
756.093 \pm 0.014	219 \pm 12	126.7 \pm 0.5	940.342 \pm 0.035	356 \pm 57	194.5 \pm 0.7
760.024 \pm 0.010	246 \pm 10	184.2 \pm 0.6	950.000 \pm 0.200	356 \pm 200	286.0 \pm 0.9
760.188 \pm 0.008	278 \pm 7	711.0 \pm 1.5	960.424 \pm 0.026	285 \pm 48	219.7 \pm 0.8
761.852 \pm 0.012	275 \pm 8	166.1 \pm 0.6	970.651 \pm 0.013	282 \pm 25	324.5 \pm 1.0
763.938 \pm 0.011	211 \pm 10	173.9 \pm 0.6	980.618 \pm 0.019	278 \pm 37	145.2 \pm 0.7
767.763 \pm 0.011	254 \pm 11	259.3 \pm 0.8	984.201 \pm 0.040	377 \pm 30	482.9 \pm 1.3
771.846 \pm 0.010	235 \pm 10	224.1 \pm 0.7	990.308 \pm 0.033	274 \pm 40	185.8 \pm 0.8
773.788 \pm 0.012	240 \pm 11	154.5 \pm 0.6	1000.350 \pm 0.220	274 \pm 58	594.0 \pm 1.5
775.057 \pm 0.013	244 \pm 12	142.2 \pm 0.5	1001.900 \pm 0.040	347 \pm 9	631.6 \pm 1.6
775.059 \pm 0.011	305 \pm 9	1063.6 \pm 2.1	1005.998 \pm 0.030	361 \pm 10	1664.4 \pm 3.2
776.019 \pm 0.010	229 \pm 9	167.1 \pm 0.6	1009.610 \pm 0.030	362 \pm 10	722.1 \pm 1.8
776.944 \pm 0.013	260 \pm 13	143.8 \pm 0.5	1015.742 \pm 0.030	391 \pm 11	627.3 \pm 1.7
777.925 \pm 0.009	316 \pm 7	1270.2 \pm 2.5	1016.843 \pm 0.021	351 \pm 16	1651.8 \pm 3.4
778.017 \pm 0.011	243 \pm 11	210.1 \pm 0.7	1017.959 \pm 0.020	374 \pm 18	1253.2 \pm 2.7
779.023 \pm 0.009	243 \pm 8	198.8 \pm 0.7	1019.101 \pm 0.011	380 \pm 8	2441.6 \pm 4.7
779.994 \pm 0.010	233 \pm 10	183.7 \pm 0.6	1019.955 \pm 0.021	409 \pm 7	2617.6 \pm 5.0
780.960 \pm 0.006	207 \pm 6	171.5 \pm 0.6	1020.932 \pm 0.040	406 \pm 9	1396.3 \pm 3.0
781.023 \pm 0.004	311 \pm 2	3706.4 \pm 6.4	1022.114 \pm 0.030	372 \pm 8	1223.3 \pm 2.7
781.898 \pm 0.008	203 \pm 8	155.5 \pm 0.6	1022.930 \pm 0.040	382 \pm 13	815.3 \pm 2.0
782.760 \pm 0.003	323 \pm 2	5042.7 \pm 8.6	1027.752 \pm 0.030	388 \pm 13	658.6 \pm 1.7
782.807 \pm 0.009	251 \pm 8	234.9 \pm 0.7	1033.822 \pm 0.030	373 \pm 15	533.7 \pm 1.5
784.019 \pm 0.030	239 \pm 21	198.7 \pm 0.7	1039.826 \pm 0.040	431 \pm 19	585.6 \pm 1.6
784.997 \pm 0.014	260 \pm 14	224.3 \pm 0.7	1049.812 \pm 0.070	448 \pm 23	627.6 \pm 1.7
785.023 \pm 0.005	327 \pm 4	4690.8 \pm 8.0	1060.030 \pm 0.050	415 \pm 24	601.5 \pm 1.7
786.090 \pm 0.012	245 \pm 11	239.2 \pm 0.7	1099.980 \pm 0.040	472 \pm 15	1407.2 \pm 3.1

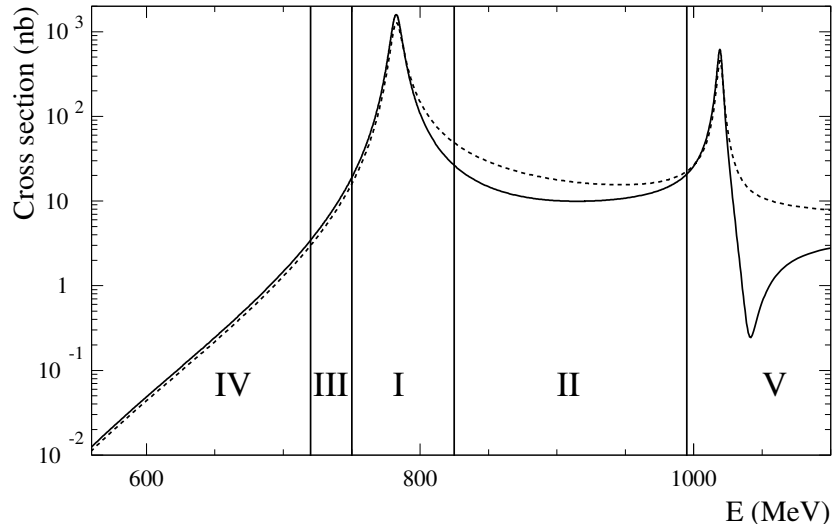


FIG. 2: The Born (solid curve) and visible (dashed curve) cross sections for the process $e^+e^- \rightarrow \pi^+\pi^-\pi^0$ in the energy region under study. The vertical lines separate five intervals in which different event selection conditions are used.

III. SELECTION OF $e^+e^- \rightarrow \pi^+\pi^-\pi^0$ EVENTS

Events of the process under study contain two charged pions and two photons from π^0 decay. About 28% of signal events contain spurious photons arising mainly from pion nuclear interaction in the calorimeter and beam background. In about 10% of events, the beam background and delta electrons lead to the appearance of additional charged tracks. Therefore, for cross section measurement we select events with two or more detected charged tracks ($n_{\text{ch}} > 1$) and two or more detected photons ($n_\gamma > 1$). At least two charged particles must originate from the collider interaction region, i.e. satisfy the conditions: $d_i < 1$ cm, $|z_i| < 15$ cm, $i = 1, 2$, and $|z_1 - z_2| < 5$ cm, where d_i is the distance between the track and the beams axis, and the z_i is the z -coordinate of the track point closest to the beam axis. The fit to a common vertex is performed using the parameters of the two charged tracks. If there are more than two charged tracks in an event satisfying the above criteria, two of them with the best χ^2 of the vertex fit are selected. The found vertex is used to refine the measured angles of charged particles and photons.

For selected events, a kinematic fit to the $\pi^+\pi^-\gamma\gamma$ hypothesis is performed with the four constraints of energy and momentum balance. The quality of the fit is characterized by

TABLE II: The selection criteria and efficiency corrections applied in energy intervals I–V.

Interval, MeV	Selection conditions	Efficiency correction
I 749 – 825	$\chi_{3\pi}^2 < 100$	1.047 ± 0.005
II 825 – 995	$\chi_{3\pi}^2 < 30$	1.056 ± 0.010
III 724 – 749	(II) and ($ \Delta\varphi > 2.3^\circ$) and ($\psi < 140^\circ$)	1.055 ± 0.010
IV 560 – 722	(III) and ($E_{\text{EMC}}/E < 0.75$) and ($\mu_{\text{veto}} = 0$) and ($n_{\text{ch}} = 2$)	1.020 ± 0.010
V 995 – 1100	(III) and ($\chi_{4\pi}^2 > 500$)	1.054 ± 0.008

the parameter $\chi_{3\pi}^2$. The photon parameters after the kinematic fit are used to calculate their invariant mass ($M_{\gamma\gamma}$). It is required to be in the range 70–200 MeV. If there are more than two photons in an event, all two-photon combinations are tested and one with $70 < M_{\gamma\gamma} < 200$ MeV and the smallest $\chi_{3\pi}^2$ is selected.

Figure 2 show the Born and visible cross sections for the process $e^+e^- \rightarrow \pi^+\pi^-\pi^0$ obtained in Sec. VI. The visible cross section is the cross section actually observed in the experiment. It takes into account radiative corrections and is related to the Born cross section $\sigma(E)$ as follows:

$$\sigma_{\text{vis}}(E) = \int_0^{x_{\text{max}}} F(x, E) \sigma(E\sqrt{1-x}) dx, \quad (1)$$

where $F(x, E)$ is a so-called radiator function [15] describing the probability to emit extra photons with the total energy $xE/2$ from the initial state, $x_{\text{max}} = 1 - (2m_{\pi^+} + m_{\pi^0})^2/E^2$.

It is seen that in the energy region under study the $e^+e^- \rightarrow \pi^+\pi^-\pi^0$ cross section changes by five orders of magnitude. We divide the energy region into five intervals, indicated in Fig. 2 by vertical lines, with very different background conditions, and use different selection criteria in them. The selection criteria are listed in Table II.

The loosest condition $\chi_{3\pi}^2 < 100$ is applied in the ω -resonance energy interval (I). The $\chi_{3\pi}^2$ distribution at the ω maximum ($E = 782.76$ MeV) is shown in Fig. 3 (left). The filled histogram represents background contribution, which is about 4%. The dashed histogram is the background distribution multiplied by a factor of 25. The number of signal and background events are determined from the fit to the $M_{\gamma\gamma}$ spectrum, in which signal events peak near π^0 mass (see Sec. IV). About 95% of background events come from the processes $e^+e^- \rightarrow e^+e^-(\gamma\gamma)$, $\mu^+\mu^-(\gamma\gamma)$, and $\pi^+\pi^-(\gamma\gamma)$, about 2% arise from $e^+e^- \rightarrow \eta\gamma$ and $\pi^0\gamma$,

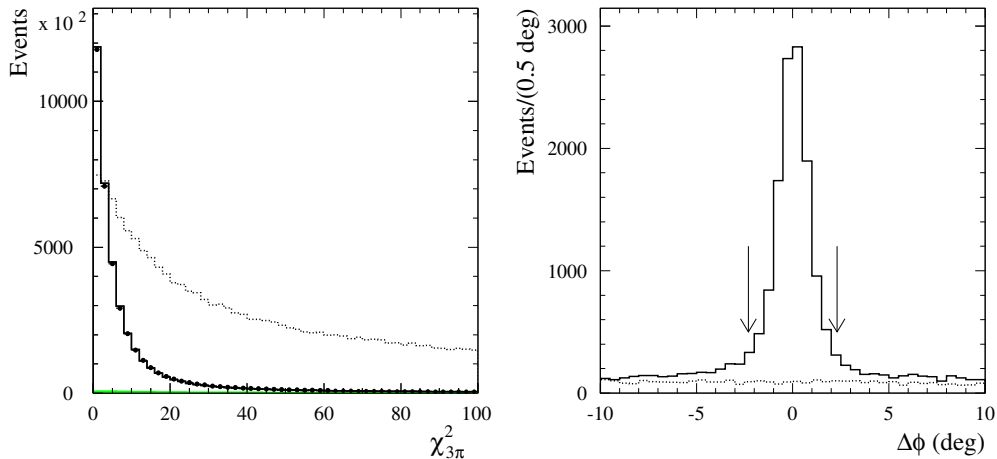


FIG. 3: Left panel: The $\chi_{3\pi}^2$ distributing for data (point with error bars) and simulated events at $E = 782.76$ MeV. The solid histogram is a sum of simulated signal and background distributions. The filled histogram represents background contribution. The dashed histogram is the background distribution multiplied by a factor of 25. Right panel: The $\Delta\varphi$ distribution for data events at $E = 719.93$ MeV (solid histogram). The dotted histogram represents the signal simulation. The arrows indicate the selection condition.

and about 3% are due to cosmic-rays.

In the energy interval between ω and ϕ resonances (II), the tighter condition $\chi_{3\pi}^2 < 30$ suppresses background and also improves the π^0 line-shape in the $M_{\gamma\gamma}$ spectrum, which is distorted by the radiative return to the ω -resonance.

To enhance the signal above the background, additional conditions are required in intervals III and IV. Figure 3 (right) shows the $\Delta\varphi = |\varphi_1 - \varphi_2| - 180^\circ$ distribution for data events and simulated $e^+e^- \rightarrow \pi^+\pi^-\pi^0$ events. The peak near $\Delta\varphi = 0$ is mainly due to $e^+e^- \rightarrow \pi^+\pi^-(\gamma)$ background events. The dotted histogram represents the signal simulation. The requirement $\Delta\varphi > 2.3^\circ$ suppresses the $e^+e^- \rightarrow \pi^+\pi^-(\gamma)$ background by a factor of about 3, while the signal loss is 3%.

Figure 4 (left) shows the distribution of the open angle between charged pions (ψ) for simulated signal and background $e^+e^-(\gamma\gamma)$ and $\pi^+\pi^-(\gamma)$ events at $E = 719.93$ MeV after applying the cut on $\Delta\varphi$. The condition $\psi < 140^\circ$ suppresses the $\pi^+\pi^-(\gamma)$ and $e^+e^-(\gamma\gamma)$ backgrounds by approximately 10 and 3 times, respectively, while the signal loss is about 30%.

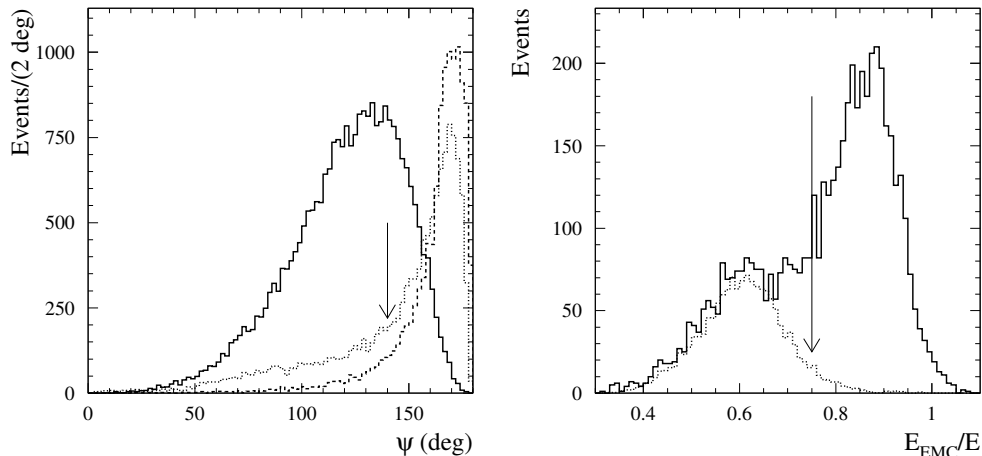


FIG. 4: Left panel: The distribution of the open angle between charged pions for simulated signal (solid histogram), $\pi^+\pi^-(\gamma)$ (dashed histogram), and $e^+e^-(\gamma\gamma)$ (dotted histogram) events at $E = 719.93$ MeV. The arrow indicates the condition $\psi < 140^\circ$. Right panel: The E_{EMC}/E distribution for data events at $E = 679.78$ MeV (solid histogram). The dotted histogram represents the signal simulation. The arrow indicates the selection condition.

After applying the conditions on $\Delta\varphi$ and ψ , the main background source in interval IV becomes the process $e^+e^- \rightarrow e^+e^-\gamma(\gamma)$. This is demonstrated in Fig. 4 (right), which shows the distribution of the normalized total energy deposition in the calorimeter (E_{EMC}/E) for data events at $E = 679.78$ MeV in comparison with the signal distribution. The peak near 0.9 is due to $e^+e^-\gamma(\gamma)$ events. The condition $E_{\text{EMC}}/E < 0.75$ suppresses this background by a factor of 6. The two additional conditions in interval IV, $\mu\text{veto} = 0$ and $n_{\text{ch}} = 2$, remove the cosmic-ray and beam-induced backgrounds. The result of sequential application of selection conditions for intervals I-IV to data events at $E = 719.93$ MeV is demonstrated in Fig. 5 (left), where the two-photon mass ($M_{\gamma\gamma}$) spectrum is shown. The improvement in the signal to background ratio is clearly seen.

In the ϕ -resonance energy range (V), additional background processes $e^+e^- \rightarrow K^+K^-$ and $e^+e^- \rightarrow K_S K_L$ appear, exhibiting a resonant energy dependence. Figure 5 (right) shows the ψ distribution at the ϕ -resonance maximum ($E = 1019.1$ MeV) for data and simulated signal and $K_S K_L$ events selected with the condition $\chi_{3\pi}^2 < 30$. The data distribution contains two peaks: near 180° due to K^+K^- events and near 150° due to $K_S K_L$ events. The condition $\psi < 140^\circ$ is used to suppress these background sources. It is seen that below 140° the data

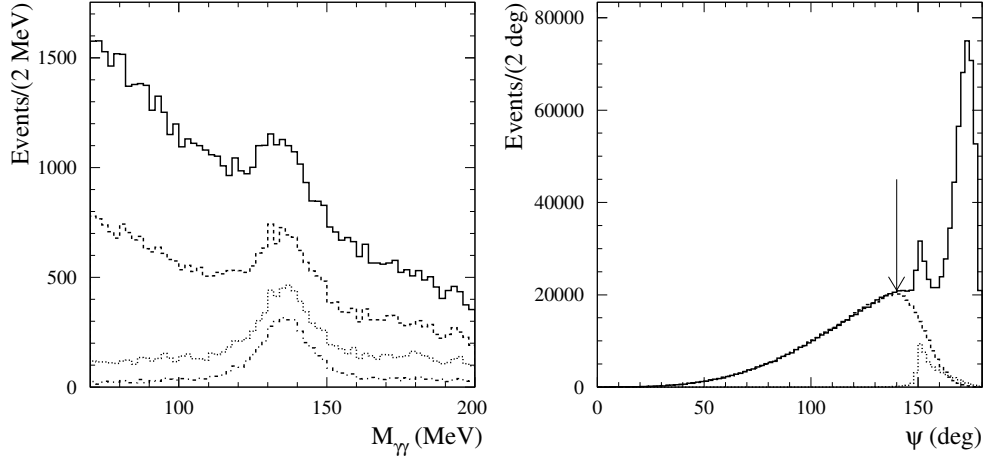


FIG. 5: Left panel: The $M_{\gamma\gamma}$ spectrum for data events at $E = 719.93$ MeV after applying the selection criteria for energy interval I (solid), II (dashed), III (dotted), and IV (dash-dotted). Right panel: The distribution of the open angle between charged pions for data (solid histogram), simulated signal (dashed histogram), and $K_S K_L$ (dotted histogram) events at $E = 1019.1$ MeV, selected with the condition $\chi_{3\pi}^2 < 30$. The arrow indicates the condition $\psi < 140^\circ$.

distribution is very close to the simulated $\pi^+\pi^-\pi^0$ distribution.

The additional nonresonant background process in the ϕ region is $e^+e^- \rightarrow \pi^+\pi^-\pi^0\pi^0$. In the energy region under study it is dominated by the $\omega\pi^0$ intermediate state. Its cross section grows almost linearly from 0.4 nb at 920 MeV to 11 nb at 1100 MeV. The fraction of $\pi^+\pi^-\pi^0\pi^0$ events in the total background for events selected with conditions III is about 40% at $E = 1000$ MeV and about 50% at $E = 1100$ MeV. Background $\pi^+\pi^-\pi^0\pi^0$ events have a broad bump near 150 MeV in the $M_{\gamma\gamma}$ spectrum, so it is desirable to suppress them. To do this we perform a kinematic fit for events with four or more detected photons to the $e^+e^- \rightarrow \pi^+\pi^-\pi^0\pi^0$ hypothesis and reject events with $\chi_{4\pi}^2 < 500$. This condition suppresses the $\pi^+\pi^-\pi^0\pi^0$ background by a factor of 2.3, while the signal loss is 4%.

IV. FITTING THE $M_{\gamma\gamma}$ DISTRIBUTION

The $M_{\gamma\gamma}$ spectra for data events are shown in Fig. 6 at four energy points, below the ω resonance ($E = 679.78$ MeV), at the ω maximum ($E = 782.76$ MeV), between the ω and ϕ resonances ($E = 920.28$ MeV), and at the ϕ maximum ($E = 1019.10$ MeV). To determine

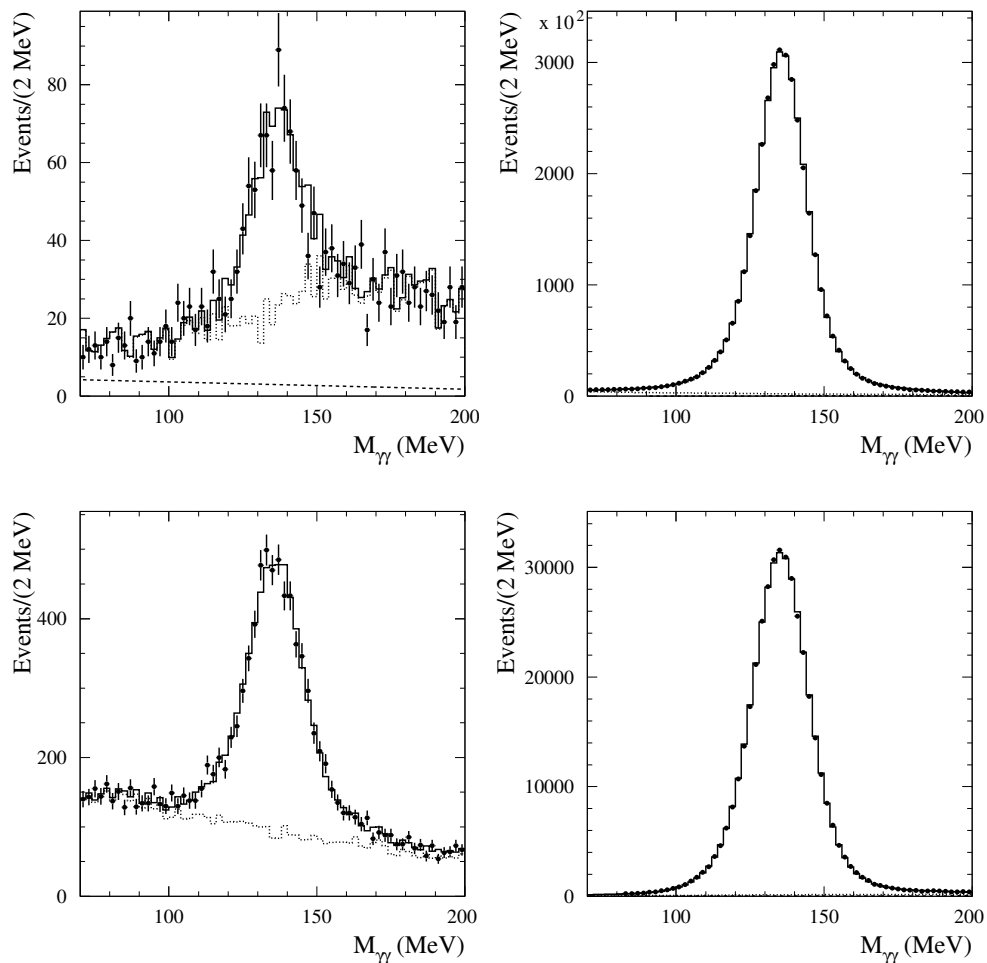


FIG. 6: The $M_{\gamma\gamma}$ spectra for selected data events (points with error bars) at $E = 679.78$ MeV (top, left), $E = 782.76$ MeV (top, right), $E = 920.28$ MeV (bottom, left), and $E = 1019.10$ MeV (bottom, right). The solid histogram represents the result of the fit described in the text. The dotted histogram is the fitted background distribution. The dashed line represents the linear component of the background.

the number of signal events ($N_{3\pi}$) at each energy point, we perform a binned likelihood fit to the $M_{\gamma\gamma}$ spectrum with a sum of signal (F_{sig}) and background (F_{bkg}) distributions.

The signal distribution is obtained by fitting the mass spectra for simulated signal events by a sum of three Gaussian functions $\epsilon_1 G_1(a_1, \sigma_1) + \epsilon_2 G_2(a_2, \sigma_2) + (1 - \epsilon_1 - \epsilon_2) G_3(a_3, \sigma_3)$. The fitted parameters are $a_1 = 136.1(136.0)$ MeV, $a_2 - a_1 = 1.6(0.8)$ MeV, $a_3 - a_1 = 9(12)$ MeV, $\sigma_1 = 7.0(8.2)$ MeV, $\sigma_2 = 12(14)$ MeV, $\sigma_3 = 30(40)$ MeV, $\epsilon_1 \approx 0.6$, $\epsilon_2 \approx 0.3$ at the maximum of the ω (ϕ) resonance. To take into account a difference between data and MC

simulation in the π^0 line shape, the signal distribution obtained in simulation is modified in the following way: $a_1^{\text{data}} = a_1^{\text{MC}} + \Delta a_1$, $a_{2,3}^{\text{data}} = a_{2,3}^{\text{MC}} + \Delta a_2$, $\sigma_{1,2,3}^{2,\text{data}} = \sigma_{1,2,3}^{2,\text{MC}} + \Delta\sigma^2$. For data points where the $N_{3\pi}$ statistical uncertainty is less than 2.5%, Δa_1 , Δa_2 , and $\Delta\sigma^2$ are free fit parameters. For the remaining points, they are fixed at the values $\Delta a_1 = -0.2 \pm 0.2$ MeV, $\Delta a_2 = -2.0 \pm 0.5$ MeV, $\Delta\sigma^2 = 3.9 \pm 1.0$ MeV². These values are obtained as averages over energy points near the ω and ϕ resonances. The uncertainties reflect their nonstatistical fluctuations. The variation of the parameters Δa_1 , Δa_2 , and $\Delta\sigma^2$ within their errors is used to estimate the associated systematic uncertainty.

A. Background distribution

The background distribution is obtained using simulation of the background processes $e^+e^- \rightarrow e^+e^-(\gamma\gamma)$, $\mu^+\mu^-(\gamma\gamma)$, $\pi^+\pi^-(\gamma)$, $\eta\gamma$, $\pi^0\gamma$, $\pi^0e^+e^-$, $\pi^+\pi^-\pi^0\pi^0$, K^+K^- , and $K_S K_L$. Analysis of the $M_{\gamma\gamma}$ distribution for events selected with the additional condition ($\mu\text{veto} = 1$) shows that the cosmic ray background is well described by a linear function. Therefore, a linear function with free parameters is added to the simulated background distribution. This linear function also serves to account for possible inaccuracies in the simulated background distribution.

We observe that the simulation underestimates the number of background events in data. Therefore, a scale factor is introduced for the expected number of events for each background process.

To determine scale factors for the main background processes $e^+e^- \rightarrow e^+e^-(\gamma\gamma)$ (S_{ee}) and $\pi^+\pi^-(\gamma)$ ($S_{\pi\pi}$), we analyze data in the energy regions 680–750 MeV and 800–920 MeV, where background contribution is relatively large. To suppress the cosmic-ray background, the condition $\mu\text{veto} = 0$ is applied. To study the dependence of the scale factors on the selection used, three sets of selection criteria are analyzed. Two of them, $\chi_{3\pi}^2 < 100$ and $\chi_{3\pi}^2 < 30$, are applied in energy intervals I and II. In the third set ($\chi_{3\pi}^2 < 30$ and $\psi < 160^\circ$), the condition on ψ is weakened compared to the standard one for intervals III-V to increase sensitivity to $S_{\pi\pi}$.

Two subsamples with $E_{\text{EMC}}/E < 0.75$ and $E_{\text{EMC}}/E > 0.75$ are analyzed to separate the $e^+e^-(\gamma\gamma)$ and $\pi^+\pi^-(\gamma)$ contributions. In both subsamples, the fit to the $M_{\gamma\gamma}$ distribution is performed, and the numbers of background events $N^{\text{data}}(E_{\text{EMC}}/E < 0.75)$ and

$N^{\text{data}}(E_{\text{EMC}}/E > 0.75)$ are determined. The scale factors are obtained by solving the system of linear equations:

$$\begin{aligned}
N^{\text{data}}(E_{\text{EMC}}/E < 0.75) &= S_{ee}N_{ee}^{\text{MC}}(E_{\text{EMC}}/E < 0.75) + S_{\pi\pi}N_{\pi\pi}^{\text{MC}}(E_{\text{EMC}}/E < 0.75) \\
&\quad + N_{\mu\mu}^{\text{MC}}(E_{\text{EMC}}/E < 0.75), \\
N^{\text{data}}(E_{\text{EMC}}/E > 0.75) &= S_{ee}N_{ee}^{\text{MC}}(E_{\text{EMC}}/E > 0.75) + S_{\pi\pi}N_{\pi\pi}^{\text{MC}}(E_{\text{EMC}}/E > 0.75) \\
&\quad + N_{\mu\mu}^{\text{MC}}(E_{\text{EMC}}/E > 0.75), \tag{2}
\end{aligned}$$

where N_{ee}^{MC} , $N_{\pi\pi}^{\text{MC}}$, and $N_{\mu\mu}^{\text{MC}}$ are the expected numbers of $e^+e^-(\gamma\gamma)$, $\pi^+\pi^-(\gamma)$ and $\mu^+\mu^-(\gamma\gamma)$ events obtained in simulation, respectively. The fraction of the $e^+e^- \rightarrow \mu^+\mu^-(\gamma\gamma)$ process in the overall background, even in energy interval IV, does not exceed 12%. Therefore, its scale factor is taken to be equal to unity. We obtain $S_{ee} = 1.25 \pm 0.10$ and $S_{\pi\pi} = 1.55 \pm 0.05$. The quoted errors are systematic and reflect the dependence of the scale factors on energy and selection conditions.

Figure 7 (left) show the $M_{\gamma\gamma}$ spectrum for data events from the energy range 679–720 MeV selected with conditions $\chi_{3\pi}^2 < 100$ and $\mu_{\text{veto}} = 0$. The obtained above scale factors are used to calculate the expected background distribution. It is seen that the background shape is not very different from linear, and the nonlinearity is well reproduced by the scaled simulation. The relatively small background nonlinearity is characteristic of energy intervals I-III and V. In interval IV the background has a more complex shape, which is also well described by the simulation, as shown in Fig. 6 (top, left). To quantify how a possible incorrectness of the background shape in simulation affects the signal yield, we compare the signal data-to-MC ratio for the conditions $\psi < 140^\circ$ and $\psi < 160^\circ$. Weakening the condition increases the background by a factor of about two, while the signal detection efficiency increases by only 30%. The change in the ratio is $(2.6 \pm 4.2)\%$ at $E = 679.78$ MeV and $-(1.3 \pm 1.3)\%$ at $E = 719.93$ MeV. We conclude that the scaled simulation describes the shape of the data background $M_{\gamma\gamma}$ distribution reasonably well.

Near the ω resonance maximum, there is background from the processes $e^+e^- \rightarrow \pi^0e^+e^-$ and $e^+e^- \rightarrow \pi^0\gamma$. In the latter process the e^+e^- pair arises from photon conversion in material before the tracking system. This background has a peak in the $M_{\gamma\gamma}$ distribution shifted by about 15 MeV relative to the π^0 mass. About 60% of the $\pi^0e^+e^-$ events with $\chi_{3\pi}^2 < 100$ have $\psi < 40^\circ$ and $E_{\text{EMC}}/E > 0.75$. The $M_{\gamma\gamma}$ spectrum for these events at $E = 782.76$ MeV is shown in Fig. 7 (right). In the fit to this spectrum, the additional

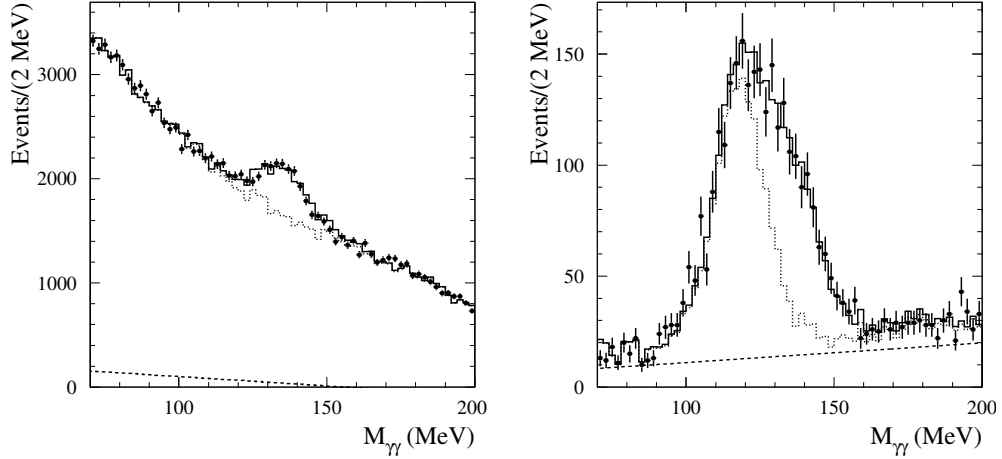


FIG. 7: Left panel: The $M_{\gamma\gamma}$ spectrum for data events (points with error bars) from the energy range 679–720 MeV selected with conditions $\chi_{3\pi}^2 < 100$ and $\mu_{\text{veto}} = 0$. The solid histogram represents the result of the fit described in the text. The dotted histogram is the fitted background distribution. The dashed line represents the linear component of the background. Right panel: The $M_{\gamma\gamma}$ spectrum for data events at $E = 782.76$ MeV (points with error bars) selected with the conditions $\chi_{3\pi}^2 < 100$, $\psi < 40^\circ$, $E_{\text{EMC}}/E > 0.75$. The solid histogram represents the result of the fit described in the text. The dotted histogram is the fitted background distribution. The peak in this distribution is due to $\pi^0 e^+ e^-$ events. The dashed line represents the linear component of the background.

parameter is introduced, the scale factor for $\pi^0 e^+ e^-$ events. It is found to be 1.11 ± 0.04 . With this scale factor the ratio of the $\pi^0 e^+ e^-$ background to the signal events selected with the condition $\chi_{3\pi}^2 < 100$ is 7×10^{-4} . The $\eta\gamma$ background is about four times smaller and have $M_{\gamma\gamma}$ distribution close to linear.

Above 920 MeV the background from the process $e^+ e^- \rightarrow \pi^+ \pi^- \pi^0 \pi^0$ must be taken into account. To find the scale factor for this process ($S_{4\pi}$), we fit to the $M_{\gamma\gamma}$ spectra for events in the energy region above 840 MeV. To increase fraction of $\pi^+ \pi^- \pi^0 \pi^0$ background, the requirement $n_\gamma > 2$ is used together with the conditions $\chi_{3\pi}^2 < 30$, $\psi < 140^\circ$, and $\mu_{\text{veto}} = 0$. In the fit to the $M_{\gamma\gamma}$ spectrum, the scale factor $S_{4\pi}$ is set to unity. The energy dependence of the cross section for the fitted background (σ_{bkg}) is shown in Fig. 8 (left). The energy points near the ϕ resonance, where there are large $K\bar{K}$ background, are removed from this plot. The background energy dependence is fitted by the function $\sigma_{\text{bkg},i}^{\text{exp}} = \sigma_{\text{non-}4\pi,i}^{\text{MC}} + S_{4\pi} \sigma_{4\pi,i}^{\text{MC}} + C$,

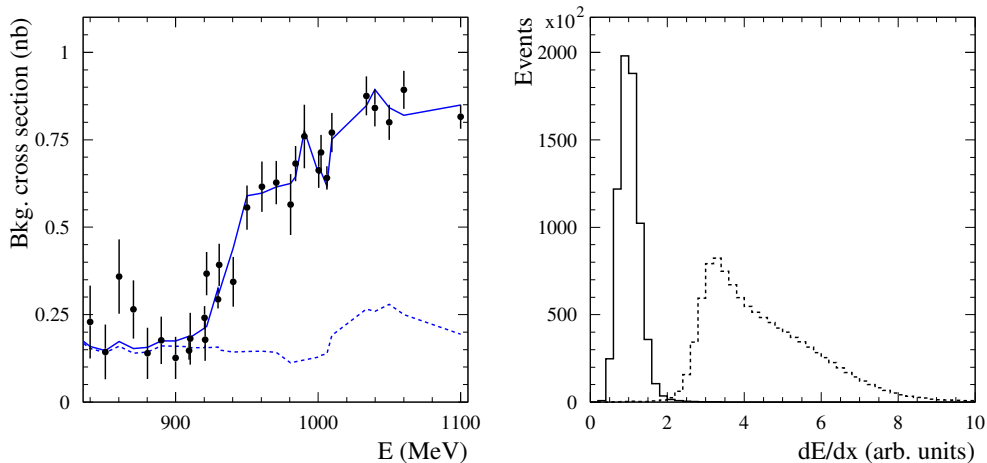


FIG. 8: Left panel: The energy dependence of background cross section for events selected with conditions $n_\gamma > 2$, $\chi_{3\pi}^2 < 30$, $\psi < 140^\circ$, and $\mu_{\text{veto}} = 0$. The solid curve is the result of the fit described in the text. The dashed curve is non- 4π background. Right panel: The distribution of ionization loss (dE/dx) in the drift chamber for charged pions from the $e^+e^- \rightarrow \pi^+\pi^-\pi^0$ reaction (solid histogram) and charged kaons from the $e^+e^- \rightarrow K^+K^-$ reaction (dashed histogram) at $E = 1019.10$ MeV.

where $\sigma_{4\pi,i}^{\text{MC}}$ and $\sigma_{\text{non-}4\pi}^{\text{MC}}$ are the expected cross sections for 4π and non- 4π backgrounds, respectively, and C is a free constant. The scale factor is found to be $S_{4\pi} = 1.03 \pm 0.04$. The consistent scale-factor value is obtained for events selected without the condition $\psi < 140^\circ$.

Near the maximum of the ϕ resonance, about 70% of background events arise from the decays $\phi \rightarrow \eta\gamma$ with $\eta \rightarrow \pi^+\pi^-\pi^0$, $\phi \rightarrow K^+K^-$, and $\phi \rightarrow K_S K_L$. To determine the scale factor for the process $e^+e^- \rightarrow \eta\gamma$ ($S_{\eta\gamma}$), we analyze a sample of events selected with the conditions for energy interval V and specific conditions ($n_\gamma > 2$, $E_{\gamma,\text{max}} > 330$ MeV, and $\mu_{\text{veto}} = 0$) that increase the fraction of $\eta\gamma$ events. The $M_{\gamma\gamma}$ spectra for events with $E = 1019.10$ MeV and $E = 1019.96$ MeV are fitted. A background distribution without a linear component, but with a free parameter $S_{\eta\gamma}$, is used in the fit. The scale factor is found to be $S_{\eta\gamma} = 1.02 \pm 0.07$.

Most $e^+e^- \rightarrow K^+K^-$ events are rejected by the condition $\psi < 140^\circ$. The remaining events typically contain a single charged kaon, while the second charged particle is a pion, muon, or electron from the second kaon decay or its nuclear interaction in the material before the drift chamber. To obtain a data sample enriched in $e^+e^- \rightarrow K^+K^-$ events,

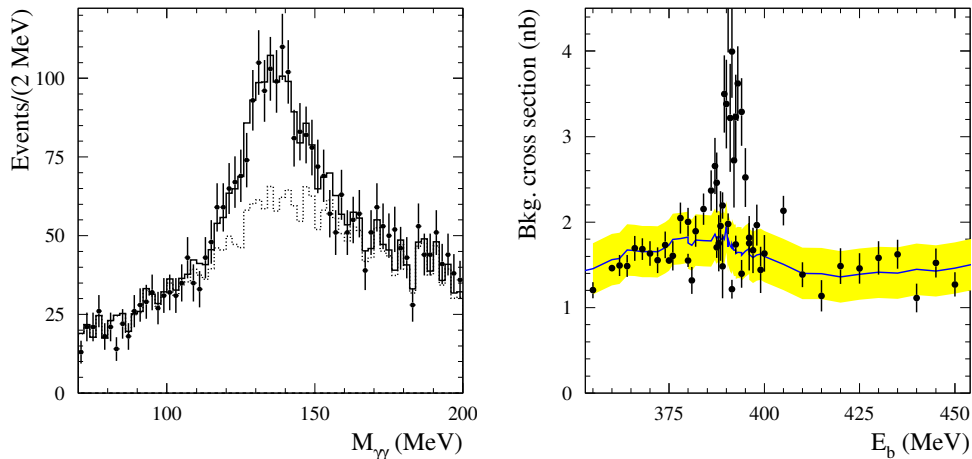


FIG. 9: Left panel: The $M_{\gamma\gamma}$ spectrum for data events at $E = 1019.10$ MeV (points with error bars), selected using the criteria for energy interval V and the condition $(dE/dx)_{\max} > 3$. The solid histogram represents the result of the fit described in the text. The dotted histogram is the fitted background distribution. Right panel: The energy dependence of the background cross section obtained from the fit to the $M_{\gamma\gamma}$ spectrum for data events selected with the conditions (3). The curve is the background cross section calculated using Eq. (4). The shaded band represents the systematic uncertainty of Eq. (4).

we use the difference in ionization losses (dE/dx) measured in the drift chamber between kaons and pions. The dE/dx distributions for charged pions from the $e^+e^- \rightarrow \pi^+\pi^-\pi^0$ reaction and charged kaons from the $e^+e^- \rightarrow K^+K^-$ reaction at $E = 1019.10$ MeV are shown Fig. 8 (right). The $M_{\gamma\gamma}$ spectrum for data events at $E = 1019.10$ MeV, selected using the criteria for energy interval V and the condition on the the maximum dE/dx for two charged tracks $(dE/dx)_{\max} > 3$, is shown in Fig. 9 (left). In the fitted background distribution, the K^+K^- background dominates. It is seen that the background distribution differs from linear. A difference in this distribution between the data and the simulation is also observed. Therefore, for the fit shown in Fig. 9 (left), the K^+K^- distribution for data events from the four energy points near the maximum of the ϕ resonance, selected with the condition $(dE/dx)_{\max} > 4.5$, is used. From the fits to the $M_{\gamma\gamma}$ spectra at $E = 1019.10$ MeV and $E = 1019.96$ MeV, the scale factor for K^+K^- events is found to be 2.00 ± 0.06 .

The scale factor for the $K_S K_L$ events ($S_{K_S K_L}$) is then found from the fit to the $M_{\gamma\gamma}$ spectrum for data events selected using the criteria for energy interval V and the condition

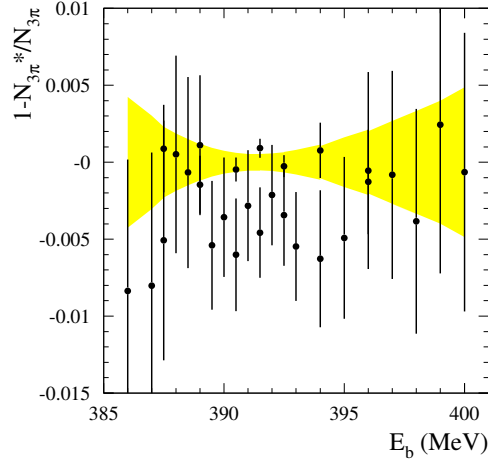


FIG. 10: Left panel: The relative difference between the number of signal events obtained by fitting the $M_{\gamma\gamma}$ spectrum and the number of signal events obtained by subtracting the background. The error bars show the statistical uncertainties, and the shaded band shows the systematic uncertainty associated with background subtraction.

$\mu_{\text{veto}} = 0$. A background distribution without a linear component, but with a free parameter $S_{K_S K_L}$, is used in the fit. All other scale factors are fixed at the values obtained above. From the fits to mass spectra at $E = 1019.10$ MeV and $E = 1019.96$ MeV, the scale factor is found to be $S_{K_S K_L} = 1.45 \pm 0.20$.

B. Systematic uncertainty in $N_{3\pi}$

The quality of the fit to the $M_{\gamma\gamma}$ spectrum at energy points with large statistics, for example, at $E = 782.76$ MeV, is poor, $\chi^2/\nu \approx 15$, where ν is the number degrees of freedom. The fractions of the linear background at two close energy points, 782.76 and 782.81 MeV, collected at different running periods, differ significantly. At these points, the gas gain in the tracking system differed by approximately a factor of 2. It can be concluded that the π^0 line shape used in the fit is not entirely correct, and the line shape in the data can vary from point to point.

To study the systematic error in $N_{3\pi}$ arising from the imperfect shape of the signal distribution, we employ an alternative background subtraction method. Events selected

with the following criteria are analyzed:

$$\chi_{3\pi}^2 < 100, \psi < 160^\circ, \mu_{\text{veto}} = 0, E_{\text{EMC}}/E < 0.75, n_{\text{ch}} = 2. \quad (3)$$

With these conditions, the background to signal ratio near the ω resonance maximum becomes less than 0.01. We perform the fit to the $M_{\gamma\gamma}$ spectra and determine the numbers of background events. Figure 9 (right) shows the energy dependence of the background cross section. Large fluctuations in the cross section near the ω resonance maximum are associated with the event transition from the signal to the background and vice versa. Away from the resonance maximum, the signal to background ratio decreases and the influence of this effect diminishes. The background cross section far from the resonance is well described by the following formula

$$\sigma_{\text{bkg}} = \sigma_{\text{bkg,exp}} + 0.2 \text{ nb}, \quad (4)$$

where $\sigma_{\text{bkg,exp}}$ is the background cross section expected from the simulation, and the constant (0.2 nb) is the contribution of the linear background. The cross section calculated using Eq. (4) is shown in Fig. 9 (right). The shaded area around the curve shows the systematic uncertainty of Eq. (4), $\Delta\sigma_{\text{bkg}} = 0.3 \text{ nb}$, conservatively estimated from the deviations of the data points from the curve at beam energies $E_b < 385 \text{ MeV}$ and $E_b > 415 \text{ MeV}$. The number of signal events can be obtained by subtracting the background calculated using Eq. (4) from the number of selected events with $70 < M_{\gamma\gamma} < 200 \text{ MeV}$. Fig. 10 shows the relative difference between the number of signal events obtained by fitting the $M_{\gamma\gamma}$ spectrum and the number of signal events obtained by subtracting the background. The error bars show the statistical uncertainties, and the shaded band shows the systematic uncertainty associated with background subtraction. The nonstatistical deviations from zero do not exceed 0.6%. This value is used as an estimate of the systematic error associated with the uncertainty of the signal shape. For energy points with small statistics, systematic uncertainties due to fixing the parameters Δa_1 , Δa_2 , and $\Delta\sigma^2$ are quadratically added to this error, which are estimated by variation of these parameters within their errors.

Figure. 10 shows that for many energy points, the fit yields a shifted value of $N_{3\pi}$. This shift can be reduced by determining the number of events ($N_{3\pi,1}$) selected with the conditions (3) by subtracting the background, as described above, and by fitting to the $M_{\gamma\gamma}$ spectrum for the remaining events with $\chi_{3\pi}^2 < 100$ ($N_{3\pi,2}$). The total number of signal events is calculated as $N_{3\pi} = N_{3\pi,1} + N_{3\pi,2}$, with the ratio $N_{3\pi,2}/N_{3\pi}$ being approximately 0.2. This

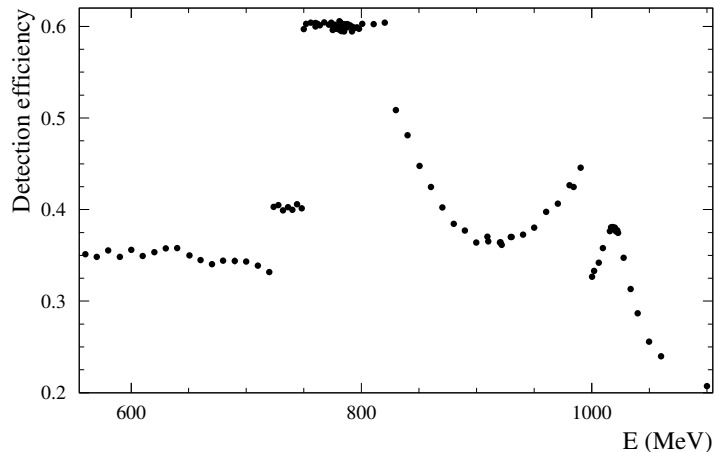


FIG. 11: The detection efficiency for $e^+e^- \rightarrow \pi^+\pi^-\pi^0$ events obtained using MC simulation.

method is used in the energy range 763.94–810.58 MeV, where its systematic uncertainty $\sqrt{(\Delta\sigma_{\text{bkg}}L)^2 + (0.006N_{3\pi,2})^2}$ does not exceed $0.006N_{3\pi}$.

To estimate the systematic error arising from uncertainty of the background shape, we modified the function describing background. Instead of a linear contribution, we introduced a common scale factor for the background obtained from the simulation. The difference between the results of fits with the two background functions is calculated. To eliminate the contribution of the cosmic-ray background, the condition $\mu_{\text{veto}} = 0$ is applied. Systematic errors due to uncertainties in the scale factors for background processes are determined by their variation within the errors. All of these contributions to the systematic uncertainty are added quadratically to the uncertainty associated with the signal line shape.

The numbers of signal events $N_{3\pi}$ obtained for different energy points with statistical and systematic errors are listed in Tables III, IV, and V. Below 720 MeV, the systematic uncertainty in $N_{3\pi}$ is dominated by the uncertainty associated with the background shape. In the range of 760–1050 MeV, it is dominated by the uncertainty associated the signal shape.

V. DETECTION EFFICIENCY

The energy dependence of the detection efficiency for $e^+e^- \rightarrow \pi^+\pi^-\pi^0$ events obtained using MC simulation is shown in Fig. 11. Five energy intervals with different selection criteria

(see Table II) are clearly visible. In the region of the ω resonance (interval I), the efficiency reaches 60%. Nonstatistical fluctuations in the efficiency observed in this interval are due to various experimental conditions (dead detector channels, beam-induced background, etc.). In intervals IV, III, and I, the efficiency exhibits a steplike behavior. A more complex energy dependence in intervals II and V is due to radiative return to the resonances ω and ϕ . Events with a hard photon emitted from the initial state are rejected by the condition $\chi_{3\pi}^2 < 30$.

The imperfect MC simulation of the detector response for charged pions and photons leads to an inaccuracy in the simulation-derived detection efficiency. Therefore, we introduce efficiency corrections. As a first step, we determine the corrections due to conditions in intervals II–V, which are additional to those in interval I. To do this, we remove one of the additional conditions used in these intervals and estimate the efficiency correction factor as $C_i = (N^{data}/N_{MC})/(N_0^{data}/N_0^{MC})$, where N^{data} (N_0^{data}) and N^{MC} (N_0^{MC}) are the numbers of signal events in the data and in the signal simulation, respectively, for the modified (nominal) selection criteria.

To determine the correction for the condition $\chi_{3\pi}^2 < 30$ ($C_{\chi_{3\pi}^2}$), we analyze three energy regions, where the radiation from the initial state is small. The correction is calculated as a weighted average over the energy points. It is found to be $C_{\chi_{3\pi}^2} = 1.004 \pm 0.004$ and 1.009 ± 0.007 near the maxima of the ϕ ($E = 1015$ – 1023 MeV) and ω ($E = 776$ – 797 MeV) resonances, respectively, and 1.013 ± 0.005 in the range $E = 719$ – 751 MeV. Due to nonstatistical fluctuations of $C_{\chi_{3\pi}^2}$ values, the uncertainties in the ϕ and ω regions are calculated as the standard deviation of the corrections at different energy points. In the latter range, the uncertainty is statistical. The corrections in different energy regions are consistent with each other. However, a slight decrease in $C_{\chi_{3\pi}^2}$ with increasing energy cannot be ruled out. To account for this possible decrease, the correction with the highest uncertainty, obtained near the ω resonance, 1.009 ± 0.007 , is used in energy intervals II and III.

The correction C_ψ , associated with the angular conditions $|\Delta\varphi| > 2.3^\circ$ and $\psi < 140^\circ$, used in intervals III, IV, V, is determined in the energy range near the ω resonance ($E = 750$ – 815 MeV). It is found to be $C_\psi = 0.9987 \pm 0.0003$. Three additional corrections in energy interval IV, associated with the conditions $E_{\text{EMC}}/E < 0.75$, $\mu_{\text{veto}} = 0$, and $n_{\text{ch}} = 2$, are $C_{\text{EMC}} = 0.981 \pm 0.003$, $C_{\mu_{\text{veto}}} = 0.998 \pm 0.002$, and $C_{n_{\text{ch}}} = 0.983 \pm 0.003$, respectively. They are obtained in the energy range $E = 695$ – 751 MeV. The additional correction in energy

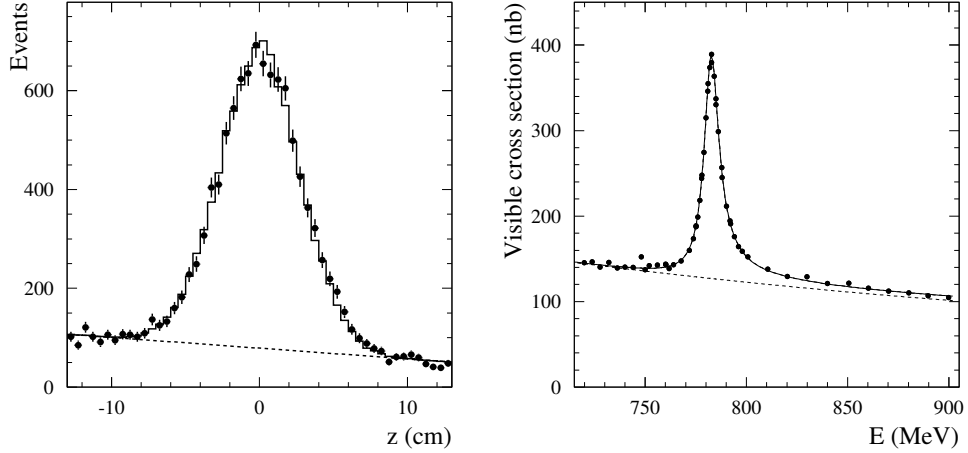


FIG. 12: Left panel: The z -distribution of the charged track with the smallest d . The solid histogram is the result of the fit described in the text. The dashed line represents the contribution of the beam-induced background. Right panel: The energy dependence of the visible cross section for selected events from C1 sample. The solid curve is the result of the fit by the sum of the ω line shape and the quadratic background. The dashed curve is the fitted background cross section.

interval V, associated with the condition $\chi_{4\pi}^2 > 500$, is equal to $C_{n_{\chi_{4\pi}^2}} = 1.0036 \pm 0.0005$.

Above, we considered efficiency corrections calculated relative to events selected with the criteria for ω meson energy range (interval I). To determine the efficiency corrections for interval I, we analyze events that do not satisfy these criteria.

A sample of events (C1) with at least two charged tracks originating from the collider interaction region, one or more photon, and $\chi_{3\pi}^2 > 100$ for events with $n_\gamma > 1$ is used to study the data-simulation difference in photon loss and the fraction of signal events rejected by the condition $\chi_{3\pi}^2 < 100$. These two effects cannot be studied separately due to the high probability of detecting a spurious photon in an event.

To suppress the cosmic-ray background and physical background mainly from $e^+e^- \rightarrow e^+e^-\gamma$ and $e^+e^- \rightarrow \pi^+\pi^-\gamma$ events, the conditions $\mu_{\text{veto}} = 0$ and $\psi < 140^\circ$ are applied. The $e^+e^- \rightarrow e^+e^-\gamma$ background is additionally suppressed by the condition $E_{\text{EMC}}/E < 0.75$. The beam-induced background is subtracted by fitting the z -distribution of the charged track with the smallest d_i . This distribution is shown in Fig. 12 (left). It is fitted by the sum of the simulated signal distribution and a linear function for the beam-induced background. From the fit, the number of beam-induced background events (N_{beam}) is obtained at each

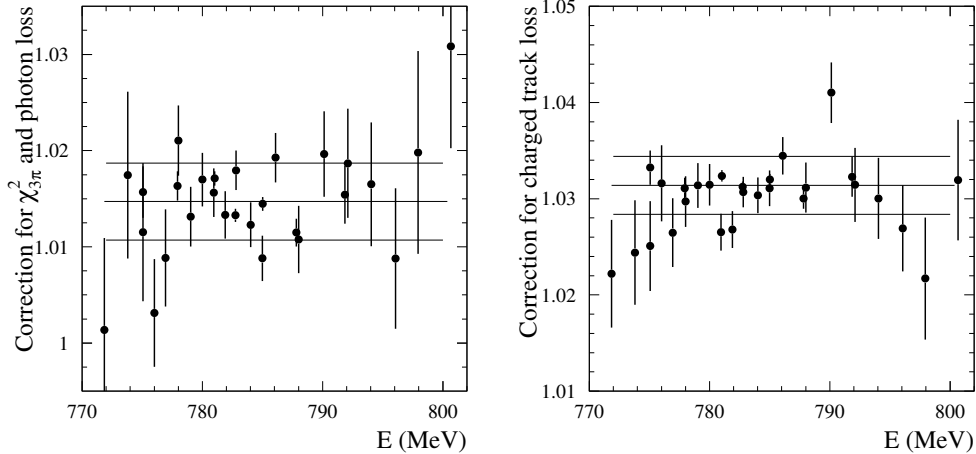


FIG. 13: The efficiency corrections for photon loss and the condition $\chi^2_{3\pi} < 100$ (left) and charged track loss (right). The middle line shows the result of the fit with a constant. The upper and lower lines show the interval $\pm 1\sigma_{\text{sys}}$.

energy point.

To determine the remaining background, we use the fact that the process $e^+e^- \rightarrow \pi^+\pi^-\pi^0$ dominates in the ω -resonance region. The energy dependence of the visible cross section for selected events after subtracting the expected $e^+e^- \rightarrow \pi^+\pi^-\gamma$ ($N_{\pi^+\pi^-\gamma}$) and $\eta\gamma$ ($N_{\eta\gamma}$) backgrounds, and the beam-induced background is shown in Fig. 12 (right). The peak of the ω -resonance from $e^+e^- \rightarrow \pi^+\pi^-\pi^0$ events is clearly seen above the almost linear background. The cross section is fitted by the sum of the ω line shape obtained in Sec. VI and the quadratic background contribution. Finally, the number of $\pi^+\pi^-\pi^0$ events at i th energy point of C1 sample is determined as

$$N_{C1,3\pi} = N_{C1} - N_{\text{beam}} - N_{\pi^+\pi^-\gamma} - N_{\eta\gamma} - \sigma_{\text{bkg}}(E_i)L_i, \quad (5)$$

where N_{C1} is the number of selected events at i th point of C1 sample, and $\sigma_{\text{bkg}}(E_i)$ is the background cross section obtained as result of the fit shown in Fig. 12 (right). For normalization, events with $\chi^2_{3\pi} < 100$, satisfying the background suppression criteria described above, are used. The number of $\pi^+\pi^-\pi^0$ events at i th energy point is determined by fitting the $M_{\gamma\gamma}$ distribution. The energy dependence of the efficiency correction for photon loss and the condition $\chi^2_{3\pi} < 100$ is shown in Fig. 13 (left). The average value is $C_\gamma = 1.015 \pm 0.004$, where the uncertainty is calculated as the standard deviation of the corrections at different points in the energy range $E = 777\text{--}795$ MeV.

A sample of events (C2) with exactly one charged track originating from the collider interaction region, and two or more photon is used to study the data-simulation difference in charged track loss. Any number of charged tracks with $d > 1$ cm or $|z| > 15$ cm is allowed.

To suppress background, the conditions $\mu_{\text{veto}} = 0$ and $100 < m_{2\gamma}^* < 170$ MeV are applied, where $m_{2\gamma}^*$ is the invariant mass of two photons with energy greater than 50 MeV, closest to the π^0 mass. To suppress the background from the $e^+e^- \rightarrow \pi^0\gamma$ and $e^+e^- \rightarrow \pi^0e^+e^-$ events, we reject events with $E_{\text{EMC}}/E > 0.8$ and $E_{\gamma,\text{max}}/E > 0.8$, where $E_{\gamma,\text{max}}$ is the energy of the most energetic photon in the event.

The beam-induced background is determined from the fit to the z -distribution for the charged track originating from the interaction region. Similar to C1 sample, we subtract the beam-induced background, and expected backgrounds from the $\pi^+\pi^-\gamma$, $\pi^0e^+e^-$, $\pi^0\gamma$, and $\eta\gamma$ events, and fit to the energy dependence of the visible cross section to determine the remaining background cross section. The same procedure is used for the normalization sample containing events with at least two charged tracks originating from the collider interaction region. The energy dependence of the efficiency correction for charged track loss is shown in Fig. 13 (right). The average value is $C_{\text{ch.tr.}} = 1.032 \pm 0.003$, where the uncertainty is calculated as the standard deviation of the corrections at different points in the energy range $E = 777\text{--}795$ MeV.

The correction $C_{\text{ch.tr.}}$ is mainly due to the difference between data and simulation in the efficiency of the tracking system at small polar angles. In particular, the simulation does not take into account the reduction in gas gain near the ends of the sensitive wires. We can estimate this effect by comparing the fractions of signal events with ($\theta_\pi < 36^\circ$ or $\theta_\pi > 144^\circ$) in data and simulation, where θ_π is the charged pion polar angle. The tracks with $36^\circ < \theta_\pi < 144^\circ$ contain more than 4 hits in the drift chamber and, therefore, are expected to have a reconstruction efficiency close to unity. We study events near the maximum of the ω resonance selected with the condition $\chi_{3\pi}^2 < 100$. Assuming unit reconstruction efficiency for tracks with $36^\circ < \theta_\pi < 144^\circ$, we obtain that the number of signal events without any polar angle constraints in the data is $(2.2 \pm 0.4)\%$ less than in the simulation.

The superimposing the charged track from the beam background on the signal event can also lead to charged track loss, which may differ between data and simulation. We study events near the maximum of the ω resonance selected with the condition $\chi_{3\pi}^2 < 100$ and observe that the fraction of signal events with $n_{\text{ch}} > 2$ in simulation ($\sim 12\%$) is larger than

that in data ($\sim 11\%$). This difference of approximately 1% can be partly explained by the difference between the data and the simulation in track loss for events with extra charged tracks.

The third effect leading to the charged track loss is nuclear interaction in material before the tracking system. The cross section of nuclear interaction strongly depends on charged pion momentum p_π . This can lead to the energy dependence of the correction $C_{\text{ch.tr.}}$. To study the possible energy dependence, we determine the corrections for events with $E_{\pi^0} > 290$ MeV and $E_{\pi^0} < 240$ MeV. The average charged pion momenta for signal events selected with these conditions are 190 MeV/ c and 240 MeV/ c , respectively. In this momentum range, the nuclear interaction cross section grows more than two times. Since we do not observe any significant difference between the corrections with $E_{\pi^0} > 290$ MeV and $E_{\pi^0} < 240$ MeV, we conclude that the nuclear interaction is reproduced by simulation correctly.

The total correction factor (C) for energy intervals I–V obtained as products of correction factors for individual conditions are listed in Table II. It is assumed that the corrections C_γ and $C_{\text{ch.tr.}}$ are independent of energy and are the same for all intervals. This assumption was verified above for the $C_{\text{ch.tr.}}$ correction. The energy dependence of C_γ can arise from a change in the shape of the $\chi_{3\pi}^2$ distribution. To estimate the value of this effect, we use the energy dependence of the $C_{\chi_{3\pi}^2}$ correction. This correction was measured at three energy points. The deviation from the value measured near the ω resonance does not exceed 0.5%. This deviation is taken as a measure of the systematic uncertainty associated with the possible energy dependence of C_γ for intervals II–V. The corrected efficiencies calculated as $\varepsilon = \varepsilon^{\text{MC}}/C$, where ε^{MC} is the efficiency obtained from the MC simulation, are listed in Tables III, IV, and V.

VI. FITTING THE MEASURED CROSS SECTION

Directly from the experiment we obtain the visible cross section

$$\sigma_{\text{vis},i} = \frac{N_{3\pi,i}}{\varepsilon_i I L_i}, \quad (6)$$

TABLE III: The center-of-mass energy (E), detection efficiency (ε), number of selected events ($N3\pi$), radiative correction ($1 + \delta$), correction for the energy spread ($1 + \delta_E$), Born cross section for the process $e^+e^- \rightarrow \pi^+\pi^-\pi^0$ (σ). The first error in the number of events and the cross section is statistical, the second is systematic.

E , MeV	ε	$N3\pi$	$1 + \delta$	$1 + \delta_E$	σ , nb
560.237	0.3440	$0.1 \pm 2.5 \pm 4.2$	0.9055	1.0000	$0.01 \pm 0.15 \pm 0.26$
570.215	0.3410	$11.1 \pm 6.0 \pm 9.3$	0.9046	1.0000	$0.47 \pm 0.26 \pm 0.40$
580.145	0.3482	$4.5 \pm 5.1 \pm 6.3$	0.9035	1.0000	$0.16 \pm 0.19 \pm 0.23$
590.206	0.3410	$0.0 \pm 2.8 \pm 5.0$	0.9023	1.0000	$0.00 \pm 0.15 \pm 0.26$
600.151	0.3486	$0.0 \pm 4.7 \pm 12.3$	0.9010	1.0000	$0.00 \pm 0.16 \pm 0.43$
610.068	0.3421	$1.2 \pm 2.9 \pm 2.3$	0.8996	1.0000	$0.06 \pm 0.15 \pm 0.12$
620.167	0.3461	$0.3 \pm 2.8 \pm 4.1$	0.8979	1.0000	$0.01 \pm 0.11 \pm 0.16$
630.085	0.3502	$1.4 \pm 3.8 \pm 5.3$	0.8962	1.0000	$0.05 \pm 0.15 \pm 0.20$
640.019	0.3504	$4.7 \pm 4.2 \pm 6.2$	0.8942	1.0000	$0.18 \pm 0.16 \pm 0.24$
650.612	0.3426	$2.8 \pm 3.9 \pm 5.7$	0.8919	1.0000	$0.11 \pm 0.15 \pm 0.23$
660.328	0.3377	$1.5 \pm 4.0 \pm 0.7$	0.8896	1.0000	$0.06 \pm 0.16 \pm 0.03$
670.201	0.3333	$5.8 \pm 4.5 \pm 1.1$	0.8869	1.0000	$0.23 \pm 0.18 \pm 0.04$
679.781	0.3370	$557.5 \pm 34.3 \pm 13.1$	0.8841	1.0000	$0.64 \pm 0.04 \pm 0.02$
689.880	0.3368	$69.3 \pm 11.2 \pm 3.0$	0.8807	1.0000	$0.82 \pm 0.13 \pm 0.04$
699.860	0.3362	$110.5 \pm 12.8 \pm 2.8$	0.8770	1.0001	$1.55 \pm 0.18 \pm 0.04$
709.969	0.3319	$118.7 \pm 12.8 \pm 4.6$	0.8726	1.0000	$2.15 \pm 0.23 \pm 0.09$
719.930	0.3250	$2348.5 \pm 56.2 \pm 27.1$	0.8676	1.0001	$3.52 \pm 0.09 \pm 0.06$
723.798	0.3818	$177.7 \pm 18.8 \pm 1.8$	0.8654	1.0001	$3.71 \pm 0.39 \pm 0.06$
727.733	0.3836	$198.5 \pm 18.2 \pm 3.4$	0.8631	1.0001	$4.83 \pm 0.45 \pm 0.10$
731.994	0.3782	$237.9 \pm 19.7 \pm 3.5$	0.8602	1.0002	$6.25 \pm 0.52 \pm 0.12$
736.202	0.3815	$413.8 \pm 25.1 \pm 6.5$	0.8571	1.0002	$7.54 \pm 0.46 \pm 0.15$
739.948	0.3790	$453.7 \pm 25.3 \pm 4.7$	0.8541	1.0001	$10.08 \pm 0.57 \pm 0.16$
744.089	0.3845	$536.4 \pm 27.0 \pm 4.1$	0.8503	1.0001	$12.71 \pm 0.65 \pm 0.18$
748.048	0.3803	$791.0 \pm 33.1 \pm 10.4$	0.8462	1.0001	$16.55 \pm 0.70 \pm 0.30$
750.019	0.5659	$49865.0 \pm 395.9 \pm 371.4$	0.8440	1.0003	$19.03 \pm 0.18 \pm 0.27$
751.989	0.5758	$1242.6 \pm 56.2 \pm 22.7$	0.8416	1.0002	$21.56 \pm 0.98 \pm 0.44$
756.093	0.5768	$1848.1 \pm 63.8 \pm 26.8$	0.8359	1.0002	$30.25 \pm 1.06 \pm 0.51$
760.024	0.5766	$3834.0 \pm 92.6 \pm 45.7$	0.8295	1.0004	$43.50 \pm 1.07 \pm 0.64$
760.188	0.5731	$14974.7 \pm 179.3 \pm 97.7$	0.8292	1.0005	$44.30 \pm 0.55 \pm 0.48$
761.852	0.5757	$4367.9 \pm 91.0 \pm 29.7$	0.8261	1.0006	$55.26 \pm 1.19 \pm 0.61$
763.938	0.5743	$5383.5 \pm 93.3 \pm 60.6$	0.8219	1.0004	$65.56 \pm 1.19 \pm 0.93$
767.763	0.5774	$13025.7 \pm 134.7 \pm 85.5$	0.8128	1.0008	$106.96 \pm 1.19 \pm 1.16$
771.846	0.5749	$20403.4 \pm 163.8 \pm 80.8$	0.8008	1.0011	$197.54 \pm 1.81 \pm 1.87$
773.788	0.5770	$19891.0 \pm 158.4 \pm 55.4$	0.7941	1.0014	$280.56 \pm 2.64 \pm 2.54$
775.057	0.5737	$23889.0 \pm 169.1 \pm 55.2$	0.7895	1.0017	$370.25 \pm 3.27 \pm 3.30$
775.059	0.5692	$178207.2 \pm 463.0 \pm 434.9$	0.7895	1.0027	$371.86 \pm 1.54 \pm 3.33$
776.019	0.5742	$34459.9 \pm 201.7 \pm 69.4$	0.7860	1.0017	$456.18 \pm 3.38 \pm 4.03$
776.944	0.5747	$36835.0 \pm 206.1 \pm 68.0$	0.7828	1.0022	$568.16 \pm 4.31 \pm 5.00$
777.925	0.5705	$412833.6 \pm 684.2 \pm 755.7$	0.7798	1.0031	$728.24 \pm 2.51 \pm 6.40$
778.017	0.5735	$69411.5 \pm 280.1 \pm 120.8$	0.7796	1.0018	$737.60 \pm 4.47 \pm 6.47$
779.023	0.5729	$83795.9 \pm 306.5 \pm 139.5$	0.7778	1.0013	$944.72 \pm 5.17 \pm 8.28$
779.994	0.5736	$96689.0 \pm 327.0 \pm 171.5$	0.7782	1.0002	$1178.99 \pm 6.32 \pm 10.36$

TABLE IV: The center-of-mass energy (E), detection efficiency (ε), number of selected events ($N3\pi$), radiative correction ($1 + \delta$), correction for the energy spread ($1 + \delta_E$), Born cross section for the process $e^+e^- \rightarrow \pi^+\pi^-\pi^0$ (σ). The first error in the number of events and the cross section is statistical, the second is systematic.

E , MeV	ε	$N3\pi$	$1 + \delta$	$1 + \delta_E$	σ , nb
780.960	0.5786	$108314.5 \pm 343.3 \pm 162.9$	0.7821	0.9990	$1396.92 \pm 6.95 \pm 12.20$
781.023	0.5692	$2331460.0 \pm 1596.6 \pm 3440.8$	0.7825	0.9977	$1415.55 \pm 2.87 \pm 12.35$
781.898	0.5771	$110880.5 \pm 346.3 \pm 161.3$	0.7910	0.9982	$1564.83 \pm 7.77 \pm 13.65$
782.760	0.5681	$3678420.0 \pm 1997.2 \pm 5338.3$	0.8047	0.9949	$1603.83 \pm 3.08 \pm 13.99$
782.807	0.5757	$172385.6 \pm 433.4 \pm 285.9$	0.8056	0.9969	$1587.08 \pm 6.56 \pm 13.91$
784.019	0.5746	$136124.9 \pm 384.6 \pm 209.9$	0.8345	0.9984	$1430.95 \pm 7.97 \pm 12.51$
784.997	0.5729	$134076.0 \pm 381.8 \pm 208.8$	0.8641	0.9997	$1207.90 \pm 5.97 \pm 10.56$
785.023	0.5679	$2737805.0 \pm 1728.1 \pm 4027.1$	0.8649	0.9996	$1188.83 \pm 2.45 \pm 10.38$
786.090	0.5753	$117118.2 \pm 358.2 \pm 191.4$	0.9013	1.0007	$943.54 \pm 4.74 \pm 8.26$
787.811	0.5721	$441148.3 \pm 699.0 \pm 691.7$	0.9640	1.0016	$662.77 \pm 1.95 \pm 5.80$
788.023	0.5754	$74116.1 \pm 287.7 \pm 130.4$	0.9719	1.0014	$618.71 \pm 3.51 \pm 5.43$
790.133	0.5742	$53766.7 \pm 249.8 \pm 124.9$	1.0499	1.0011	$404.24 \pm 2.64 \pm 3.60$
791.856	0.5677	$124984.0 \pm 381.5 \pm 266.0$	1.1119	1.0014	$301.75 \pm 1.34 \pm 2.67$
792.108	0.5728	$36237.8 \pm 206.4 \pm 79.8$	1.1208	1.0009	$289.36 \pm 2.21 \pm 2.57$
794.047	0.5715	$32269.8 \pm 197.0 \pm 87.9$	1.1876	1.0009	$214.76 \pm 1.80 \pm 1.95$
796.067	0.5719	$28212.8 \pm 186.6 \pm 86.6$	1.2538	1.0006	$165.92 \pm 1.53 \pm 1.52$
797.955	0.5706	$16295.7 \pm 144.7 \pm 72.5$	1.3125	1.0003	$132.80 \pm 1.67 \pm 1.29$
800.668	0.5757	$18382.6 \pm 155.2 \pm 75.1$	1.3914	1.0002	$101.38 \pm 1.26 \pm 0.97$
810.583	0.5755	$15882.5 \pm 147.3 \pm 105.1$	1.6283	1.0001	$50.09 \pm 0.78 \pm 0.54$
820.284	0.5768	$11700.6 \pm 148.9 \pm 74.9$	1.7901	1.0001	$32.09 \pm 0.74 \pm 0.35$
829.859	0.4815	$4792.0 \pm 94.2 \pm 35.4$	1.8930	1.0000	$23.24 \pm 0.87 \pm 0.34$
840.025	0.4555	$3190.0 \pm 78.6 \pm 22.1$	1.9525	1.0000	$18.29 \pm 0.89 \pm 0.26$
850.553	0.4240	$3475.3 \pm 84.9 \pm 23.9$	1.9721	1.0000	$15.49 \pm 0.75 \pm 0.22$
860.252	0.4022	$1790.8 \pm 59.2 \pm 13.4$	1.9618	1.0000	$13.01 \pm 0.85 \pm 0.19$
870.291	0.3811	$2331.8 \pm 70.0 \pm 23.9$	1.9303	1.0000	$11.83 \pm 0.69 \pm 0.19$
880.194	0.3640	$1684.1 \pm 58.9 \pm 12.7$	1.8848	1.0000	$11.30 \pm 0.75 \pm 0.17$
889.788	0.3570	$1510.3 \pm 56.7 \pm 11.4$	1.8316	1.0000	$9.65 \pm 0.67 \pm 0.14$
899.816	0.3448	$1815.6 \pm 62.0 \pm 12.6$	1.7703	1.0000	$9.98 \pm 0.61 \pm 0.14$
909.399	0.3508	$8084.0 \pm 144.1 \pm 70.9$	1.7088	1.0000	$9.80 \pm 0.30 \pm 0.15$
910.112	0.3459	$1069.7 \pm 45.9 \pm 7.7$	1.7042	1.0000	$10.47 \pm 0.77 \pm 0.15$
920.282	0.3447	$5394.0 \pm 112.7 \pm 39.8$	1.6377	1.0000	$10.42 \pm 0.36 \pm 0.15$
920.685	0.3451	$1343.8 \pm 51.0 \pm 9.9$	1.6350	1.0000	$10.64 \pm 0.66 \pm 0.16$
921.726	0.3421	$1603.1 \pm 56.9 \pm 12.6$	1.6282	1.0000	$10.17 \pm 0.59 \pm 0.15$
929.637	0.3505	$8247.2 \pm 141.5 \pm 60.5$	1.5763	1.0000	$10.21 \pm 0.28 \pm 0.15$
930.427	0.3504	$1432.1 \pm 54.4 \pm 13.8$	1.5711	1.0000	$9.60 \pm 0.58 \pm 0.15$
940.342	0.3529	$1102.3 \pm 47.6 \pm 7.4$	1.5062	1.0000	$10.66 \pm 0.70 \pm 0.15$
950.000	0.3602	$1571.9 \pm 55.9 \pm 13.0$	1.4423	1.0000	$10.58 \pm 0.55 \pm 0.16$
960.424	0.3763	$1275.9 \pm 48.5 \pm 11.8$	1.3716	1.0000	$11.25 \pm 0.59 \pm 0.17$
970.651	0.3850	$1989.7 \pm 60.9 \pm 16.2$	1.2979	1.0000	$12.27 \pm 0.49 \pm 0.18$
980.618	0.4041	$1090.6 \pm 42.7 \pm 9.1$	1.2183	1.0000	$15.26 \pm 0.74 \pm 0.23$
984.201	0.4021	$3540.0 \pm 81.2 \pm 22.3$	1.1869	1.0001	$15.36 \pm 0.43 \pm 0.21$
990.308	0.4221	$1508.8 \pm 50.1 \pm 9.9$	1.1285	1.0001	$17.05 \pm 0.65 \pm 0.24$

TABLE V: The center-of-mass energy (E), detection efficiency (ε), number of selected events ($N3\pi$), radiative correction ($1 + \delta$), correction for the energy spread ($1 + \delta_E$), Born cross section for the process $e^+e^- \rightarrow \pi^+\pi^-\pi^0$ (σ). The first error in the number of events and the cross section is statistical, the second is systematic.

E , MeV	ε	$N3\pi$	$1 + \delta$	$1 + \delta_E$	σ , nb
1000.348	0.3101	$4944.2 \pm 79.3 \pm 32.4$	1.0139	1.0002	$26.47 \pm 0.55 \pm 0.33$
1001.900	0.3160	$5657.0 \pm 83.7 \pm 41.4$	0.9934	1.0004	$28.52 \pm 0.45 \pm 0.37$
1005.998	0.3244	$19858.6 \pm 154.7 \pm 128.8$	0.9351	1.0009	$39.30 \pm 0.37 \pm 0.49$
1009.610	0.3397	$12404.9 \pm 120.7 \pm 75.2$	0.8779	1.0019	$57.49 \pm 0.63 \pm 0.70$
1015.742	0.3572	$38647.4 \pm 207.8 \pm 232.1$	0.7702	1.0118	$221.32 \pm 2.50 \pm 2.70$
1016.843	0.3610	$146106.0 \pm 403.7 \pm 884.2$	0.7528	1.0103	$322.18 \pm 2.83 \pm 3.94$
1017.959	0.3613	$162634.0 \pm 426.1 \pm 976.7$	0.7427	0.9996	$483.82 \pm 3.73 \pm 5.91$
1019.101	0.3607	$399890.0 \pm 669.4 \pm 2400.0$	0.7573	0.9721	$616.77 \pm 1.73 \pm 7.53$
1019.955	0.3609	$386590.0 \pm 656.9 \pm 2321.3$	0.8004	0.9822	$520.51 \pm 3.40 \pm 6.36$
1020.932	0.3569	$145488.0 \pm 404.4 \pm 873.5$	0.8871	1.0118	$325.29 \pm 5.77 \pm 3.97$
1022.114	0.3580	$75822.0 \pm 292.4 \pm 457.7$	1.0378	1.0158	$164.23 \pm 2.18 \pm 2.01$
1022.930	0.3552	$36257.0 \pm 204.1 \pm 217.9$	1.1708	1.0143	$105.42 \pm 1.73 \pm 1.29$
1027.752	0.3296	$8375.4 \pm 101.0 \pm 55.2$	2.7558	1.0039	$13.95 \pm 0.47 \pm 0.19$
1033.822	0.2972	$3037.1 \pm 64.2 \pm 19.6$	11.6589	1.0009	$1.64 \pm 0.40 \pm 0.03$
1039.826	0.2721	$2192.1 \pm 55.3 \pm 16.6$	59.3097	1.0005	$0.23 \pm 0.35 \pm 0.06$
1049.812	0.2428	$1650.2 \pm 51.3 \pm 11.9$	18.4148	1.0001	$0.59 \pm 0.34 \pm 0.11$
1060.030	0.2274	$1233.9 \pm 46.2 \pm 15.9$	7.5355	1.0000	$1.20 \pm 0.34 \pm 0.14$
1099.980	0.1968	$2313.6 \pm 65.8 \pm 25.5$	2.7744	1.0000	$3.01 \pm 0.24 \pm 0.21$

where i is the number of the energy point. It is related to the Born cross section $\sigma(E)$ by Eq. (1), which can be rewritten in the conventional form:

$$\sigma_{vis}(E) = \int_0^{x_{max}} F(x, E) \sigma(E\sqrt{1-x}) dx = \sigma(E)(1 + \delta(E)), \quad (7)$$

where $\delta(E)$ is the radiative correction.

To take into account the beam energy spread, it is necessary to perform a convolution of the visible cross section (7) with a Gaussian describing the c.m. energy distribution of the electron-positron pair. Since the energy spread is much smaller than the width of the ω and ϕ resonances, we use an approximate formula instead of convolution,

$$\sigma_{vis}(E) \implies \sigma_{vis}(E) + \frac{1}{2} \frac{d^2 \sigma_{vis}}{dE^2}(E) \sigma_E^2 = \sigma_{vis}(E)(1 + \delta_E(E)) \quad (8)$$

To obtain the experimental Born cross section, the visible cross section data are fitted using a model for $\sigma(E)$ that describe the data well. Using the fitted model parameters, the

radiative and energy spread corrections are calculated. The Born cross section at the energy point i is then determined as

$$\sigma_i = \frac{N_{3\pi,i}}{\varepsilon_i I L_i (1 + \delta_i)(1 + \delta_{E,i})}, \quad (9)$$

The uncertainty in the collider energy listed in Table I effectively increases the uncertainty in the measured visible cross section. When fitting the cross section energy dependence, the following term is added in quadrature to the statistical error of $\sigma_{\text{vis},i}$:

$$\delta E_i \frac{d\sigma_{\text{vis}}}{dE}(E_i), \quad (10)$$

where δE_i is the uncertainty in the energy of i th point.

To describe the Born cross section, the VMD model is used, which includes the amplitudes of the ρ , ω , and ϕ mesons and an amplitude that takes into account the contribution of the higher vector resonances:

$$\begin{aligned} \sigma_{3\pi}(E) &= \frac{12\pi}{E^3} |F(E)|^2 P_{\rho\pi}(E) \\ F(E) &= \sum_{V=\rho,\omega,\phi,\omega'} \frac{\Gamma_V m_V^{3/2} \sqrt{\mathcal{B}(V \rightarrow e^+e^-)\mathcal{B}(V \rightarrow 3\pi)}}{D_V(E)} \frac{e^{i\varphi_V}}{\sqrt{P_{\rho\pi}(m_V)}}, \end{aligned} \quad (11)$$

where m_V and Γ_V are the mass and width of the resonance V , φ_V is its phase, and $\mathcal{B}(V \rightarrow e^+e^-)$ and $\mathcal{B}(V \rightarrow 3\pi)$ are the branching fractions of V into e^+e^- and 3π ,

$$\begin{aligned} D_V(E) &= m_V^2 - E^2 - iE\Gamma_V(E), \\ \Gamma_V(E) &= \sum_f \Gamma_f(E). \end{aligned} \quad (12)$$

Here $\Gamma_f(E)$ is the mass-dependent partial width of the resonance decay into the final state f , and $\Gamma_f(m_V) = \Gamma_V \mathcal{B}(V \rightarrow f)$. The mass-dependent width for the ω and ϕ mesons has been calculated taking into account all significant decay modes. The corresponding formulae can be found, for example, in Ref. [6]. We assume that the $V \rightarrow 3\pi$ decay proceeds via the $\rho\pi$ intermediate state, and $P_{\rho\pi}(E)$ is the 3π phase space volume calculated under this hypothesis. The formula for the $P_{\rho\pi}$ calculation can be found in Ref. [6].

The phase φ_ω is set to zero. Thus, all other phases φ_V represent relative phases between the amplitudes of the V and ω resonances. In general, they depend on energy, for example, due to vector meson mixing. Since the value of the form factor $F(E)$ at $E = 0$ is a real number determined by the $\gamma \rightarrow 3\pi$ chiral anomaly (see, for example, Ref. [23]), all phases

TABLE VI: The fitted VMD model parameters in comparison with the PDG data [25] and results of Refs. [6] and [7] for φ_ϕ and φ_ρ , respectively.

Parameter	Fitted value	PDG value
$\mathcal{B}(\omega \rightarrow e^+e^-)\mathcal{B}(\omega \rightarrow 3\pi) \times 10^5$	$6.648 \pm 0.022 \pm 0.058$	6.61 ± 0.16
m_ω , MeV	$782.703 \pm 0.011 \pm 0.047$	782.66 ± 0.13
Γ_ω , MeV	$8.598 \pm 0.023 \pm 0.004$	8.68 ± 0.13
$\mathcal{B}(\phi \rightarrow e^+e^-)\mathcal{B}(\phi \rightarrow 3\pi) \times 10^5$	$4.154^{+0.102}_{-0.066} \pm 0.066$	4.42 ± 0.11
m_ϕ , MeV	$1019.488 \pm 0.017 \pm 0.061$	1019.460 ± 0.016
Γ_ϕ , MeV	$4.265 \pm 0.033 \pm 0.014$	4.249 ± 0.013
φ_ϕ , deg	$156.8^{+6.5}_{-4.6} \pm 1.9$	163 ± 7
$\mathcal{B}(\rho \rightarrow 3\pi) \times 10^5$	$4.7 \pm 1.2 \pm 1.3$	9 ± 4
φ_ρ , deg	$-95.3 \pm 8.3 \pm 4.0$	-99 ± 17

tend to 0° or 180° when the energy goes to 0. For the energy dependence of φ_ϕ , there is a theoretical prediction [24]. The phase has a minimum of about 160° at the maximum of the ϕ resonance and increases with decreasing energy. At the ω mass it is approximately 179° .

In our nominal fit, we use only the data obtained in this article, and the contribution of the excited vector resonances is modeled by a single resonance ω' with mass and width equal to the Particle Data Group (PDG) values for the $\omega(1420)$ [25]. The parameter $\varphi_{\omega'}$ is set to its expected value of 180° [26].

The free fit parameters are $\mathcal{B}(\omega \rightarrow e^+e^-)\mathcal{B}(\omega \rightarrow 3\pi)$, m_ω , $\Gamma_\omega(m_\omega)$, $\mathcal{B}(\phi \rightarrow e^+e^-)\mathcal{B}(\phi \rightarrow 3\pi)$, m_ϕ , $\Gamma_\phi(m_\phi)$, φ_ϕ , $\mathcal{B}(\rho \rightarrow 3\pi)$, φ_ρ , $\mathcal{B}(\omega' \rightarrow e^+e^-)\mathcal{B}(\omega' \rightarrow 3\pi)$. This model is close to those used to fit the data in previous measurements [3–7].

Fitting the data with purely statistical uncertainties yields $\chi^2/\nu = 167/93$. The poor quality of the fit is explained by the presence of uncorrelated systematic uncertainties. These uncertainties manifest themselves, for example, as nonstatistical fluctuations between energy points in the correction factors C_γ and $C_{\text{ch.tr.}}$ in Fig. 13. We estimate the value uncorrelated systematic uncertainty from the error of the product $C_\gamma C_{\text{ch.tr.}}$ (0.5%), and the error associated with the signal shape in the fit to the $M_{\gamma\gamma}$ spectrum (0.6%). It is 0.52% in the energy range 763.94–810.58 MeV, where the alternative method of background subtraction is used, and 0.78% outside this range. Adding these uncertainties to the statistical uncertainties of

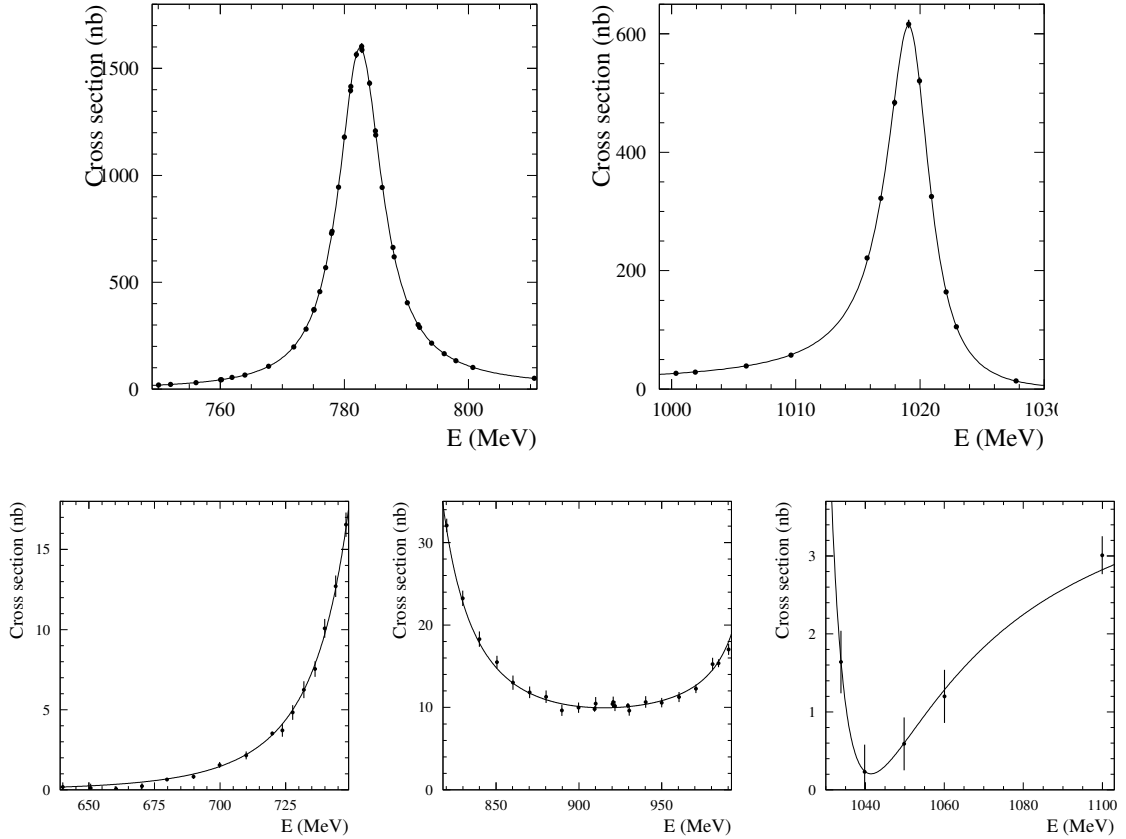


FIG. 14: The measured Born cross section for the process $e^+e^- \rightarrow \pi^+\pi^-\pi^0$ in five energy regions. The error bars represent combined statistical and systematic uncertainties. The curve is the result of the fit described in the text.

$N_{3\pi}$ in quadrature, we obtain a reasonable value of $\chi^2/\nu = 96/93$.

The fit results are used to calculate the radiative correction and the energy spread correction. The measured energy dependence of the Born cross section is shown in Fig. 14 together with the fitted curve.

The parameters of the ρ , ω , and ϕ resonances obtained from the fit to the visible cross section data are listed in Table VI in comparison with PDG values [25] and results of Refs. [6] and [7] for φ_ϕ and φ_ρ , respectively. The quoted errors are statistical and systematic. The systematic error in the masses m_ω and m_ϕ is completely determined by the systematic uncertainty in the collider energy measurement. To determine the systematic uncertainties for other parameters, we shift all IL_i , $\sigma_{E,i}$, $N_{3\pi,i}$, or efficiency corrections up and down by the value of the systematic uncertainty. To determine the model uncertainties of the

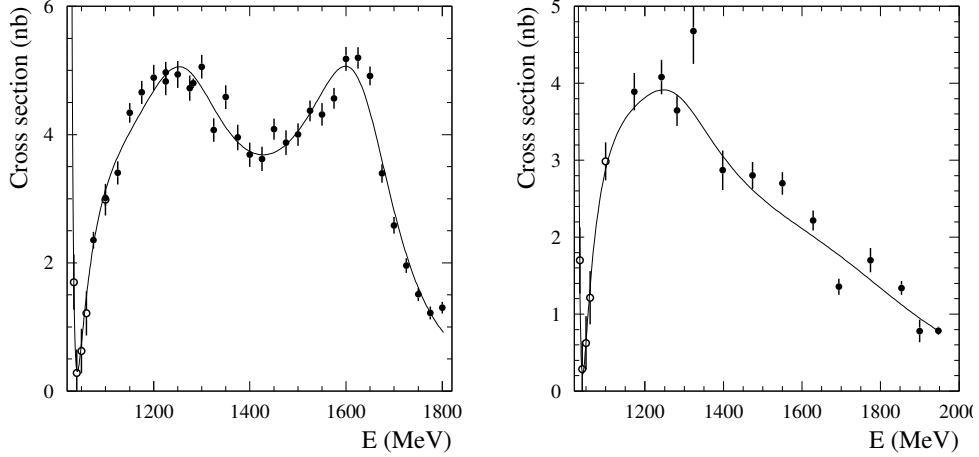


FIG. 15: The total $e^+e^- \rightarrow \pi^+\pi^-\pi^0$ cross section (left) and the cross section for $e^+e^- \rightarrow \rho\pi$ (right) measured in Ref. [27]. The curves are the results of the fits described in the text.

parameters, three alternative fit models are tested.

In model 1, instead of the constant φ_ϕ , the energy-dependent quantity $\varphi_\phi(E)$ [24] is used, multiplied by the free parameter a_ϕ . The model describes the cross section data well. The fitted value $a_\phi = 0.96 \pm 0.03$. In this model, the significant, 0.9%, decrease of the fitted value of $\mathcal{B}(\phi \rightarrow e^+e^-)\mathcal{B}(\phi \rightarrow 3\pi)$ is observed.

In the second and third models we include to the fit the cross section data obtained by SND above 1.1 GeV [27]. In this energy region, in addition to $\rho\pi$, the intermediate mechanisms $\omega\pi^0$ and $\rho(1450)\pi$ are significant. In Ref. [27], the total $e^+e^- \rightarrow \pi^+\pi^-\pi^0$ cross section, and the cross section for the mechanisms $\rho\pi$ and $\rho(1450)\pi$ were measured. It was shown that the process $e^+e^- \rightarrow \omega(1650) \rightarrow \pi^+\pi^-\pi^0$ is dominated by the intermediate mechanism $\rho(1450)\pi$. It should be noted that the Dalitz distributions for the $\rho\pi$ and $\rho(1450)\pi$ intermediate states below 0.95 GeV are not distinguishable, and the amplitudes of the ω and ρ resonances and the low-energy tail of the $\omega(1650)$ amplitude are coherent. The total contribution (including interference) of the isovector intermediate state $\omega\pi^0$ to the $e^+e^- \rightarrow \pi^+\pi^-\pi^0$ cross section reaches 16% at $E = 1.4$ GeV. However, it decreases very rapidly with decreasing energy and can be neglected below the $\omega\pi^0$ threshold of 920 MeV.

The total $e^+e^- \rightarrow \pi^+\pi^-\pi^0$ cross section and the cross section for $e^+e^- \rightarrow \rho\pi$ measured in Ref. [27] are shown in Fig. 15. To take into account intermediate states other than $\rho\pi$, the formula (11) must be modified. However, in our case, where data above 1.1 GeV are

used only to estimate the model uncertainties of the fitted parameters, a simplified approach can be applied. Assuming the intermediate $\rho\pi$ mechanism, we include in the fit either the $e^+e^- \rightarrow \rho\pi$ data (model 2) or the $e^+e^- \rightarrow \pi^+\pi^-\pi^0$ data (model 3) above 1.1 GeV. In model 2, the contribution of the $\omega(1650) \rightarrow \rho(1450)\pi$ amplitude to the $e^+e^- \rightarrow \pi^+\pi^-\pi^0$ cross section is neglected. In contrast, in model 3, the contribution of the $\omega(1650)$ amplitude is overestimated. In both models, the cross section above 1.1 GeV is described by contributions of two resonances with phases $\varphi_{\omega'} = 180^\circ$ and $\varphi_{\omega''} = 0^\circ$. The fitting curves are shown in Fig. 15. In model 3, the fitted resonance masses and widths are close to the PDG values for $\omega(1420)$ and $\omega(1650)$ [25]. In model 2, the fitted parameters of the first resonance, $m_{\omega'} = 1400 \pm 25$ MeV and $\Gamma_{\omega'} = 710 \pm 90$ MeV, do not contradict the PDG values for $\omega(1420)$, the $\omega(1650)$ contribution is not needed, instead a very broad structure with $m_{\omega''} = 2550 \pm 130$ MeV and $\Gamma_{\omega''} = 8000 \pm 3000$ MeV is additionally required to describe the $e^+e^- \rightarrow \rho\pi$ data above 1.6 GeV. The differences between parameters of the ρ , ω , and ϕ resonances obtained in the nominal model and models 1, 2 and 3 are taken as estimates of the model uncertainties. The model uncertainties determine the systematic errors of the parameters φ_ϕ , $\mathcal{B}(\rho \rightarrow 3\pi)$, and φ_ρ , and contribute to the errors of Γ_ω and $\mathcal{B}(\phi \rightarrow e^+e^-)\mathcal{B}(\phi \rightarrow 3\pi)$.

The obtained parameters of the ω meson listed in Table VI are consistent with the PDG values [25], but are much more accurate. The values of the ϕ mass and width agree with the PDG data [25], but have worse accuracy. The value of $\mathcal{B}(\phi \rightarrow e^+e^-)\mathcal{B}(\phi \rightarrow 3\pi)$ is smaller but consistent within errors with the PDG value [25]. The phase φ_ϕ agrees with the only previous measurement [6]. The accuracy of $\mathcal{B}(\rho \rightarrow 3\pi)$ and φ_ρ are improved compared with the most accurate previous BABAR measurement [7].

The values of the measured Born cross section together with the values of $(1 + \delta)$ and $(1 + \delta_E)$ are listed in in Tables III, IV, and V. The statistical uncertainty of the cross section includes the statistical uncertainties of $N_{3\pi}$, ε , and IL , and the uncertainty associated with the beam energy measurement, calculated using Eq. (10). The systematic uncertainty of the cross section includes the systematic uncertainties in the luminosity measurement (0.7%), number of signal events, detection efficiency, and radiative correction. The latter is determined by comparing the radiative corrections obtained in the nominal model and models 1, 2, and 3, and is significant at five energy points with $E > 1033$ MeV. At the maximum of the ω (ϕ) resonance, the systematic uncertainty of the cross section is 0.9% (1.2%) and significantly exceeds the statistical uncertainty.

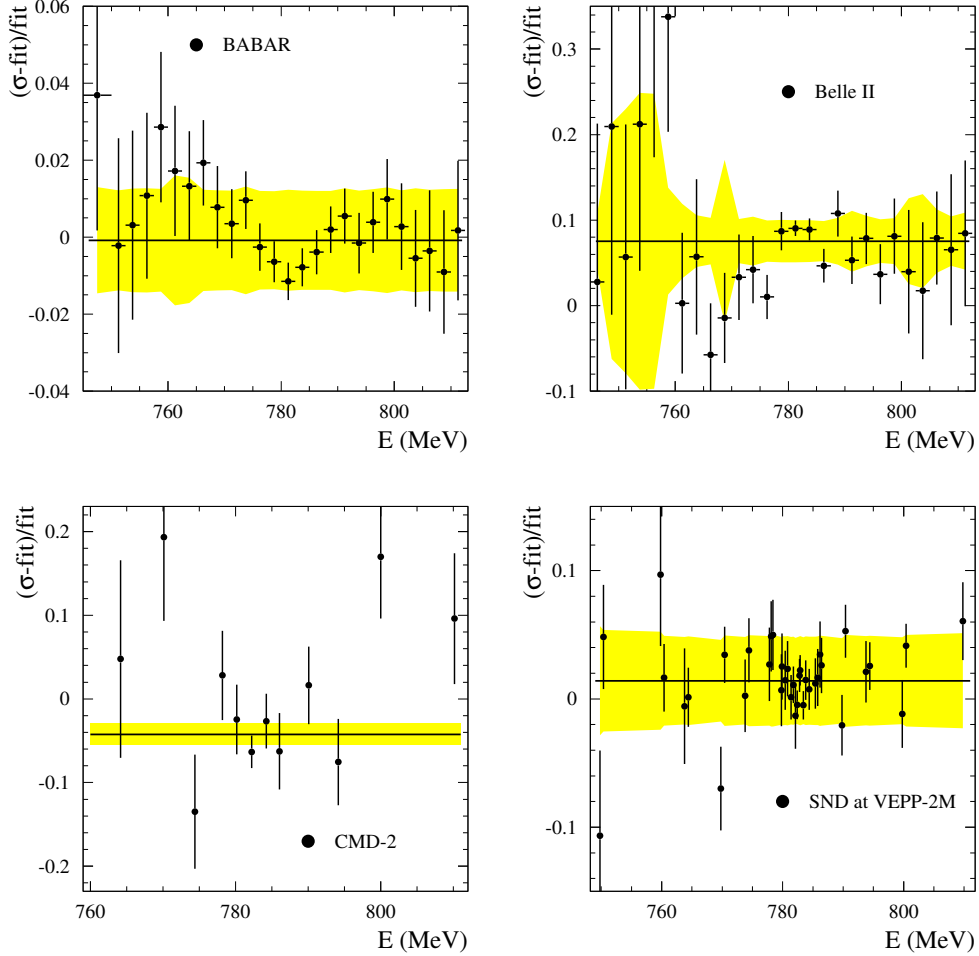


FIG. 16: The ratios of the cross sections measured in the BABAR [7] (top, left), Belle II [8] (top, right), CMD-2 [3] (bottom, left), and SND at VEPP-2M [6] (bottom, right) experiments to the cross section obtained by fitting the data from this work with the VMD model in the ω resonance energy region. The solid line represents the result of the fit to the data with a constant. The shaded band shows the systematic uncertainty of the data.

VII. COMPARISON WITH PREVIOUS MEASUREMENTS

A comparison of our results with previous measurements is presented in Figs. 16, 17, and 18, which plot the ratios of the cross sections measured in Refs. [3–8] to the cross section obtained by fitting the data from this work in the VMD model. The solid line shows the fit of the ratio energy dependence by a constant. Our measurement is in reasonable agreement with the BABAR data [7] over the entire energy range, with the SND at VEPP-2M data [6]

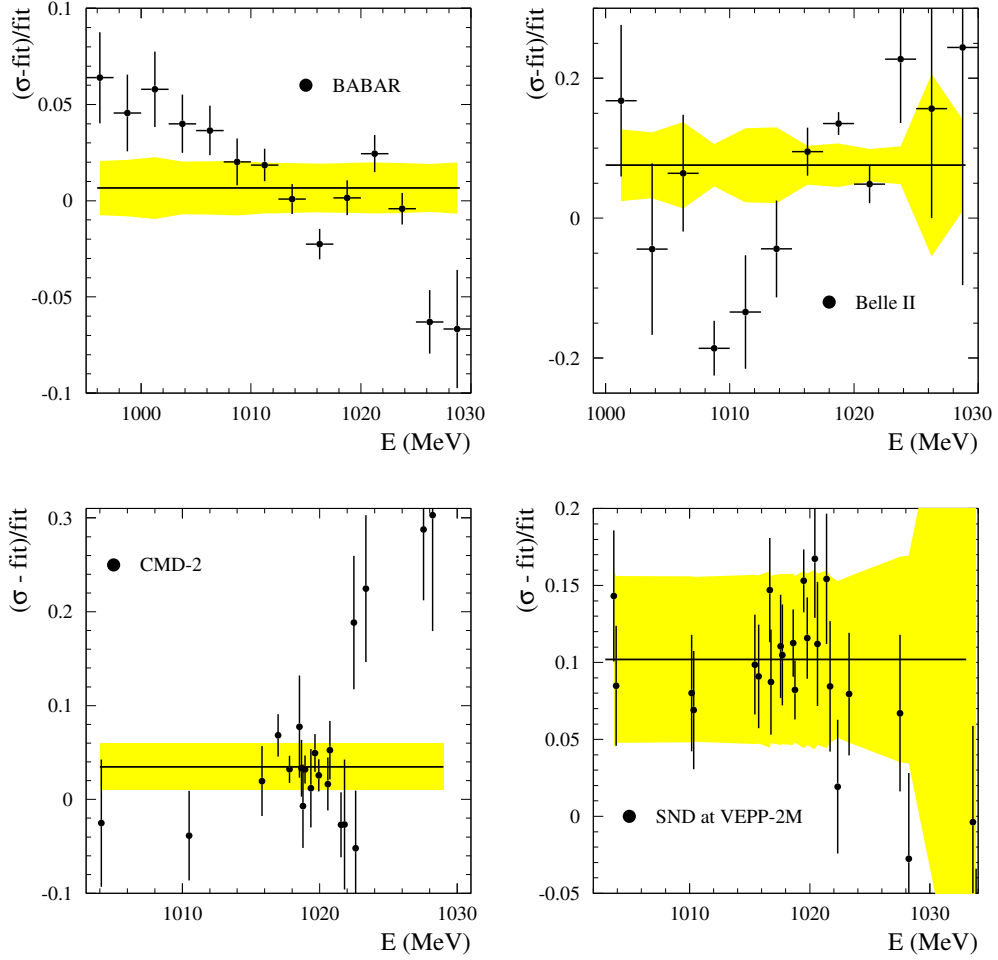


FIG. 17: The ratios of the cross sections measured in the BABAR [7] (top, left), Belle II [8] (top,right), CMD-2 [4] (bottom, left), and SND at VEPP-2M [6](bottom, right) experiments to the cross section obtained by fitting the data from this work with the VMD model in the ϕ resonance energy region. The solid line represents the result of the fit to the data with a constant. The shaded band shows the systematic uncertainty of the data.

below the ϕ resonance, with the Belle-II [8] between ω and ϕ , and with the CMD-2 data [4] near the ϕ resonance. The ratio of the Belle-II measurement to our measurement is about 1.075 near the ω and ϕ resonances. The significance of this deviation is about 2σ . In the ω energy region our measurement about 4% (2σ) larger than the CMD-2 [3] results, while in the ϕ energy region it is about 10% (2σ) lower than the SND at VEPP-2M measurement.

Using the measured $e^+e^- \rightarrow \pi^+\pi^-\pi^0$ Born cross section ($\sigma(s)$) we can calculate the 3π

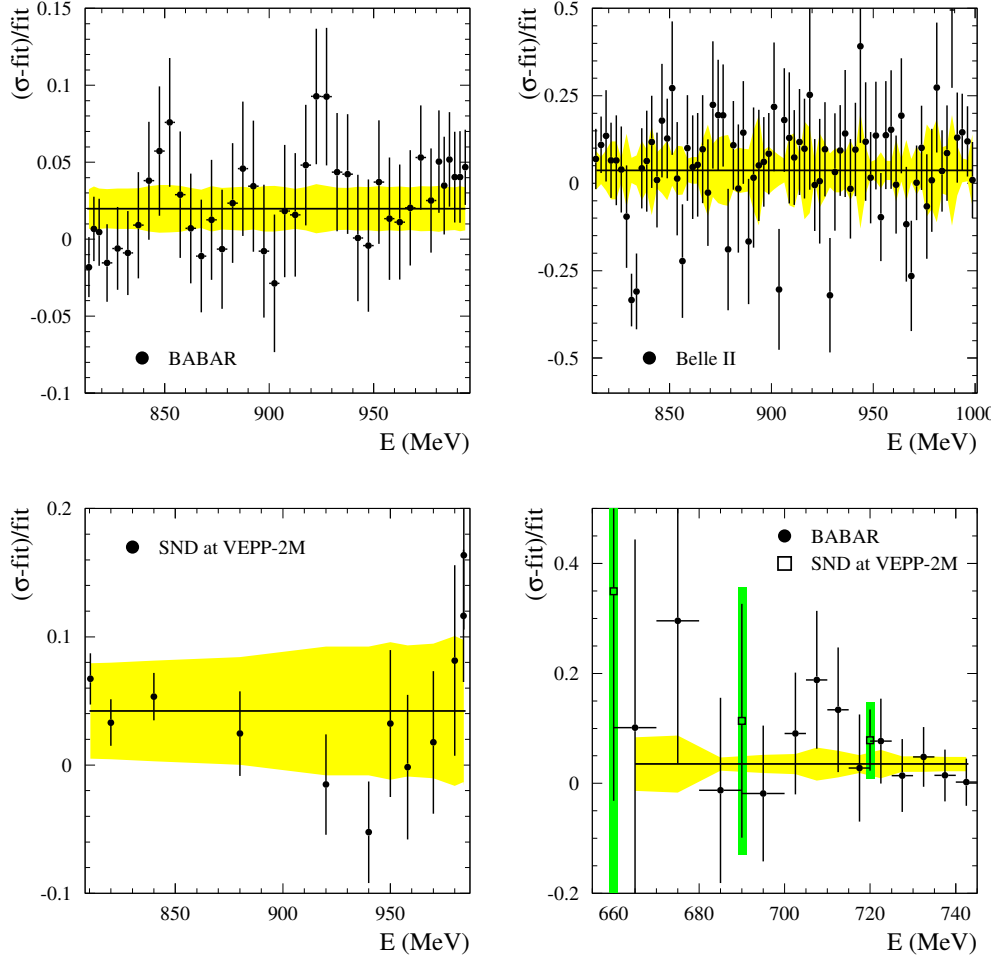


FIG. 18: The ratios of the cross sections measured in the BABAR [7] (top, left), Belle II [8] (top, right), and SND at VEPP-2M [6] (bottom, left) experiments to the cross section obtained by fitting the data from this work with the VMD model in the energy region between ω and ϕ resonances. The bottom right panel shows the same plot for the BABAR [7] and SND at VEPP-2M [6] data. The solid line represents the result of the fit to the data with a constant. The shaded band shows the systematic uncertainty of the data.

contribution to the muon anomalous magnetic moment

$$a_{\mu}^{3\pi} = \frac{\alpha^2}{3\pi^2} \int_{m_{\pi}^2}^{\infty} \frac{K(s) \sigma(s) |1 - \Pi(s)|^2}{s \cdot 4\pi\alpha^2/s} ds, \quad (13)$$

where the kernel function $K(s)$ can be found in Ref. [28] and the vacuum polarization operator $\Pi(s)$ is tabulated in Ref. [29].

Since the $e^+e^- \rightarrow \pi^+\pi^-\pi^0$ cross section contains two narrow resonance peaks, numerical

integration of Eq. (13) over the data points in Tables III, IV, and V using simple methods, such as the trapezoidal rule or Simpson's rule, do not provide the required accuracy. Therefore, the $a_\mu^{3\pi}$ calculation is performed using the theoretical cross section [Eq. (11)] with fitted parameters. The result for the energy region 0.61-1.1 GeV is listed in Table VII with statistical and systematic uncertainties.

The statistical uncertainty in $a_\mu^{3\pi}$ is obtained using pseudo-experiments (toy MC), where numbers of observed signal events are generated using the fitted function. They are fluctuated according to the data statistical and uncorrelated systematic (see Sec. VI) uncertainties, and the uncertainties in the collider energy [see Eq. (10)].

The systematic uncertainty in $a_\mu^{3\pi}$ is estimated by simultaneously increasing or decreasing the number of observed events in all data points by the amount of systematic error. The systematic uncertainty listed in Tables III, IV, and V includes an uncorrelated component. However, we cannot confidently exclude it from the total uncertainty to obtain the correlated component. Therefore, the total systematic uncertainty is conservatively used to estimate the systematic uncertainty in $a_\mu^{3\pi}$. We also study the dependence of the $a_\mu^{3\pi}$ result on the fitting model. Calculations are performed for all models considered in Sec. VI. Deviations from the nominal $a_\mu^{3\pi}$ value given in Table VII do not exceed 0.005×10^{-10} .

The contribution to $a_\mu^{3\pi}$ from the energy region 1.1–1.975 GeV is calculated using the SND data obtained in Ref. [27]. In this case the integral (13) is evaluated by using the trapezoidal rule. The obtained $a_\mu^{3\pi}$ for the energy region 1.1–1.975 GeV and for region 0.61–1.975 are listed in Table VII, where they are compared with the results of previous measurements.

The SND values of $a_\mu^{3\pi}$ for $E < 1.1$ GeV and $E > 1.1$ GeV are in good agreement with the BABAR measurements [7]. The SND value for $E < 1.975$ GeV agrees well with the result of Ref.[30] based on $e^+e^- \rightarrow \pi^+\pi^-\pi^0$ data obtained before 2021 [3–6, 31, 32], but are 2.5σ smaller than the Belle II measurement [8].

VIII. CONCLUSION

In the SND experiment at the VEPP-2000 collider, the measurement of the $e^+e^- \rightarrow \pi^+\pi^-\pi^0$ cross section has been performed in the center-of-mass energy range from 560 to 1100 MeV. Our measurement is the most accurate to date. Its systematic uncertainty is 0.9% at maximum of the ω resonance and 1.2% at maximum of the ϕ resonance. The SND

TABLE VII: Values of $a_\mu^{3\pi}$ for different energy intervals. The first three rows represent the SND results. The next three show the BABAR results [7]. The seventh row is the Belle II result [8], while the last row is the calculation [30] based on the fit to $e^+e^- \rightarrow \pi^+\pi^-\pi^0$ data obtained before 2021 [3–6, 31, 32].

E , GeV	$a_\mu^{3\pi} \times 10^{10}$
0.62–1.10 (SND)	$42.96 \pm 0.06 \pm 0.45$
1.10–1.975 (SND)	$2.99 \pm 0.02 \pm 0.08$
0.62–1.975 (SND)	$45.95 \pm 0.06 \pm 0.46$
0.62–1.10 (BABAR)	$42.91 \pm 0.14 \pm 0.55 \pm 0.09$
1.10–2.00 (BABAR)	$2.95 \pm 0.03 \pm 0.16$
< 2.00 (BABAR)	$45.86 \pm 0.14 \pm 0.58$
0.62–1.80 (Belle II)	$48.91 \pm 0.23 \pm 1.07$
< 1.8 [30]	$46.2 \pm 0.6 \pm 0.6$

measurement is in the reasonable agreement with the BABAR measurement [7], but about 7–8% smaller than the Belle II data. The leading-order hadronic contribution to the muon magnetic anomaly, calculated using the $e^+e^- \rightarrow \pi^+\pi^-\pi^0$ cross section measured by SND in this work and in Ref. [27] is $(45.95 \pm 0.06 \pm 0.46) \times 10^{-10}$ for the energy interval 0.62-1.975 GeV. Our $a_\mu^{3\pi}$ is in good agreement with the BABAR result [7] and calculation [30] based on $e^+e^- \rightarrow \pi^+\pi^-\pi^0$ data obtained before 2021 [3–6, 31, 32], but is more precise. The difference with the $a_\mu^{3\pi}$ value obtained by Belle II [8] is 2.5σ .

From the fit to the cross section data with the vector meson dominance model, the parameters of the ω , ρ , and ϕ resonances have been obtained. The obtained values of $\mathcal{B}(\omega \rightarrow e^+e^-)\mathcal{B}(\omega \rightarrow 3\pi)$, mass and width of the ω meson, and $\mathcal{B}(\rho \rightarrow 3\pi)$ have accuracy better than the PDG world average values [25].

[1] P. Y. Shatunov *et al.* Phys. Part. Nucl. Lett. **13**, 995 (2016).

[2] M. Davier, A. Hoecker, B. Malaescu and Z. Zhang, Eur. Phys. J. C **80**, 241 (2020) [erratum: Eur. Phys. J. C **80**, 410 (2020)].

- [3] R. R. Akhmetshin *et al.* (CMD-2 Collaboration), Phys. Lett. B **578**, 285 (2004).
- [4] R. R. Akhmetshin *et al.* (CMD-2 Collaboration), Phys. Lett. B **642**, 203 (2006).
- [5] M. N. Achasov *et al.* (SND Collaboration), Phys. Rev. D **63**, 072002 (2001).
- [6] M. N. Achasov *et al.* (SND Collaboration), Phys. Rev. D **68**, 052006 (2003).
- [7] J. P. Lees *et al.* (BABAR Collaboration), Phys. Rev. D **104**, 112003 (2021).
- [8] I. Adachi *et al.* (Belle-II Collaboration), Phys. Rev. D **110**, 112005 (2024).
- [9] M. N. Achasov *et al.*, Nucl. Instrum. Meth. A **449**, 125 (2000).
- [10] V. M. Aulchenko *et al.*, Nucl. Instrum. Meth. A **598**, 102 (2009).
- [11] A. Y. Barnyakov *et al.*, Nucl. Instrum. Meth. A **598**, 163 (2009).
- [12] V. M. Aulchenko *et al.*, Nucl. Instrum. Meth. A **598**, 340 (2009).
- [13] M. Ablikim *et al.* (BESIII Collaboration), Phys. Rev. D **98**, 112007 (2018).
- [14] A. Aloisio *et al.* [KLOE], Phys. Lett. B **561**, 55 (2003) [erratum: Phys. Lett. B **609**, 449 (2005)].
- [15] E. A. Kuraev and V. S. Fadin, Sov. J. Nucl. Phys. **41**, 466 (1985).
- [16] G. Bonneau and F. Martin, Nucl. Phys. B **27**, 381 (1971).
- [17] E. Barberio and Z. Was, Comput. Phys. Commun. **79**, 291 (1994).
- [18] G. V. Fedotovitch and A. L. Sibidanov, Nucl. Phys. B Proc. Suppl. **131**, 9 (2004).
- [19] G. Balossini, C. M. Carloni Calame, G. Montagna, O. Nicrosini and F. Piccinini, Nucl. Phys. B **758**, 227 (2006).
- [20] J. Allison *et al.* (GEANT Collaboration), Nucl. Instr. Meth. A **835**, 186 (2016).
- [21] E. V. Abakumova *et al.*, Nucl. Instrum. Meth. A **744**, 35 (2014).
- [22] M. N. Achasov *et al.* (SND Collaboration), JHEP **01**, 113 (2021).
- [23] M. Hoferichter, B. L. Hoid and B. Kubis, JHEP **2025**, 095 (2025).
- [24] N. N. Achasov and A. A. Kozhevnikov, Phys. Rev. D **61**, 054005 (2000); Phys. Atom. Nucl. **63**, 1936 (2000).
- [25] S. Navas *et al.* (Particle Data Group), Phys. Rev. D **110**, 030001 (2024).
- [26] A. B. Clegg and A. Donnachie, Z. Phys. C **62**, 455 (1994).
- [27] M. N. Achasov *et al.* (SND Collaboration), Phys. Atom. Nucl. **87**, 747 (2024).
- [28] T. Aoyama *et al.* Phys. Rept. **887**, 1 (2020).
- [29] F. Ignatov, <https://cmd.inp.nsk.su/ignatov/vpl>.
- [30] M. Hoferichter, B. L. Hoid and B. Kubis, JHEP **2019**, 137 (2019).

- [31] B. Aubert *et al.* (BABAR Collaboration), Phys. Rev. D **70**, 072004 (2004).
- [32] V. M. Aul'chenko *et al.* (SND Collaboration), J. Exp. Theor. Phys. **121**, 27 (2015).